# Analyzing Simulated Convective Bursts in Two Atlantic Hurricanes. Part I: Burst Formation and Development

ANDREW T. HAZELTON[a]

*Department of Earth, Ocean and Atmospheric Science, The Florida State University, Tallahassee, Florida*

ROBERT F. ROGERS

*NOAA/AOML/Hurricane Research Division, Miami, Florida*

ROBERT E. HART

*Department of Earth, Ocean and Atmospheric Science, The Florida State University, Tallahassee, Florida*

(Manuscript received 15 July 2016, in final form 21 April 2017)

ABSTRACT

Understanding the structure and evolution of the tropical cyclone (TC) inner core remains an elusive challenge in tropical meteorology, especially the role of transient asymmetric features such as localized strong updrafts known as convective bursts (CBs). This study investigates the formation of CBs and their role in TC structure and evolution using high-resolution simulations of two Atlantic hurricanes (Dean in 2007 and Bill in 2009) with the Weather Research and Forecasting (WRF) Model.

Several different aspects of the dynamics and thermodynamics of the TC inner-core region are investigated with respect to their influence on TC convective burst development. Composites with CBs show stronger radial inflow in the lowest 2 km, and stronger radial outflow from the eye to the eyewall around $z = 2$–4 km, than composites without CBs. Asymmetric vorticity associated with eyewall mesovortices appears to be a major factor in some of the radial flow anomalies that lead to CB development. The anomalous outflow from these mesovortices, along with outflow from supergradient parcels above the boundary layer, favors low-level convergence and also appears to mix high-$\theta_e$ air from the eye into the eyewall. Analyses of individual CBs and parcel trajectories show that parcels are pulled into the eye and briefly mix with the eye air. The parcels then rapidly move outward into the eyewall, and quickly ascend in CBs, in some cases with vertical velocities of over 20 m s$^{-1}$. These results support the importance of horizontal asymmetries in forcing extreme asymmetric vertical velocity in tropical cyclones.

## 1. Introduction

The inner-core structure of tropical cyclones (TCs) continues to be a key area of research in tropical meteorology. Recent work has uncovered important aspects of the evolution of the core structure, such as secondary eyewall formation (e.g., Willoughby et al. 1982; Kossin and Sitkowski 2009) and asymmetric radial flow (e.g., Reasor et al. 2013; DeHart et al. 2014, hereafter D14). However, there are many features in the eyewall and rainband region that remain poorly understood or difficult to observe. One such feature is convective bursts (CBs), anomalously strong updrafts in the eyewall and rainbands. Several recent studies have implicated these as a key component of inner-core structure, tied to both TC genesis and intensity changes (e.g., Hendricks et al. 2004; Rogers et al. 2013). Although some convective forcing mechanisms have been proposed, the details of the dynamic and thermodynamic mechanisms that lead to CB formation (and how those mechanisms vary spatially) are still not fully understood. Studies indicate that these localized updrafts can be an important feature in TC intensification (e.g., Kelley et al. 2004; Guimond et al. 2010; Rogers et al. 2013); thus, further investigation of their structure and evolution is warranted.

[a] Current affiliation: Program in Atmospheric and Oceanic Science, Princeton University, and NOAA/GFDL, Princeton, New Jersey.

*Corresponding author*: Andrew Hazelton, andy.hazelton.1003@gmail.com

DOI: 10.1175/MWR-D-16-0267.1

Past observational studies have examined various aspects of convective development within the TC inner core. Malkus and Riehl (1960) were among the first to introduce the concept of narrow "hot towers." Jorgensen et al. (1985) later supported this idea by showing that eyewall updraft "cores" were stronger and transported more mass than rainband updrafts. Black et al. (2002) discussed the role of shear in controlling the locations where updrafts strengthen and weaken, showing that updrafts tended to be concentrated in the downshear-left region (as a result of shear-induced asymmetric flow). Corbosiero and Molinari (2002) used lightning data to show a similar downshear-left preference for convective initiation. Eastin et al. (2005) used aircraft observations from two hurricanes to analyze the distribution of inner-core buoyancy. As in other studies, they found that buoyancy tended to be maximized downshear because of the shear-induced tranverse secondary circulation. Consistent with this result and subsequent studies (e.g., Reasor et al. 2013, D14), vertical velocity was also maximized downshear (particularly downshear left), with the precipitation maximum to the left of shear. Eastin et al. (2005) also used dropsonde data to infer that the low-level high-$\theta_e$ air in the eye was a primary buoyancy source for the eyewall. Barnes and Fuentes (2010) and Dolling and Barnes (2012) used dropsonde data to support this buoyancy argument. D14 constructed composites of radial flow for intense updrafts and downdrafts in each shear-relative quadrant, and found that the secondary circulation tended to be stronger for the intense updrafts, with stronger low-level inflow and upper-level outflow. The study did not determine whether the strong updrafts were a cause or a result of this circulation pattern, however. Guimond et al. (2016) used High-Altitude Imaging Wind and Rain Airborne Profiler (HIWRAP) retrievals from the NASA Global Hawk taken during the Genesis and Rapid Intensification Processes (GRIP) experiment (Braun et al. 2013) and NOAA P-3 data from the Intensity Forecast Experiment (IFEX; Rogers et al. 2013) to show that CBs formed in Hurricane Karl (2010) through convergence and buoyancy generated by air mixing between the eye and the eyewall due to mesovortices.

Modeling studies have also investigated TC convective development. Braun (2002), in an MM5 simulation of Hurricane Bob (1991), showed that eyewall convection was primarily driven by convective instability as a result of two buoyancy sources: 1) surface fluxes and 2) air flowing out from the low-level warm core in the eye into the eyewall. Braun et al. (2006) found that eyewall vertical motion in Hurricane Bonnie (1998) was largely driven by eyewall mesovortices in a background shear-relative flow. Observational evidence of such mesovortices has been documented in other studies (e.g., Aberson et al. 2004; Kossin and Schubert 2004; Hendricks et al. 2012). The dynamics associated with these structures (breakdown of a barotropically unstable eyewall) are described by Schubert et al. (1999) and Kossin and Schubert (2001). In a convection-allowing simulation of Hurricane Erin (2001), Braun and Wu (2007) found that vertical motion was driven more by mesovortices in weaker shear and also exhibited a wavenumber-1 asymmetry in stronger shear. Nguyen et al. (2011) also discussed the relationship between vortex asymmetry and eyewall convection in a simulation of Hurricane Katrina (2005), finding that vortical hot towers (VHTs) tended to develop at the vertices of an asymmetric eyewall. This development of VHTs was part of what that study termed vacillation cycles, wherein the eyewall fluctuated between an asymmetric and a symmetric state. Cram et al. (2007) used the Bonnie simulation of Braun et al. (2006) to demonstrate the presence of eye–eyewall exchange leading to buoyant eyewall air parcels, consistent with the observations discussed above. The mixing concept was further supported by a study of the relationship between eyewall convection and lightning in Hurricane Rita by Fierro and Reisner (2011), who found that strong convection was associated with eyewall asymmetry and eye–eyewall mixing.

While several studies have proposed different mechanisms for the development of convective updrafts in the eyewall region (including eyewall asymmetry and eye–eyewall exchange), it is not clear which mechanisms are dominant in generating the most extreme updrafts. In addition, the factors controlling the radial distribution of CBs have not been thoroughly investigated. Studies such as Rogers et al. (2015) have suggested that differences in the location of radial convergence in the boundary layer may be responsible, but this mechanism has not been systematically tested. In addition, the small-scale and transient nature of CBs makes them difficult to observe and resolve with current airborne and remotely sensed data. These questions and deficiencies will be addressed by analyzing simulations of real TCs using a high-resolution numerical model. Such simulations will allow finer temporal and spatial scales than are allowed by most observations, in addition to permitting the analysis of a full range of variables that may not be available observationally. This analysis will give insight into the role of small-scale asymmetric features in the evolution of larger-scale TC structure, helping to further parse out the important differences between symmetric and asymmetric dynamics. In the first part of this two-part paper, we will address CB formation, and

Hazelton et al. (2017, hereafter Part II) will then analyze the intensity change due to CBs.

## 2. Data and methodology

### a. Model configuration

This study uses version 3.6 of the Advanced Research version of the Weather Research and Forecasting Model (WRF-ARW; Skamarock and Klemp 2008). The National Centers for Environmental Prediction (NCEP) Global Forecast System (GFS) 0.5° analyses are used for the initial and boundary conditions. No bogus vortex is used, so the first part of each simulation (12 h for Dean and 36 h for Bill, with output every 15 min) is not included in later analyses, to account for spinup. Bill's vortex was weaker and more difficult to track during spinup, which is why a longer period was used. The model grids consist of a fixed outer nest with 18-km grid spacing and two inner nests that move with and are centered on the TC (Michalakes et al. 2005): the outer grid with 6-km grid spacing and the inner grid with 2-km grid spacing. Such a resolution should be expected to produce a more realistic eyewall than slightly lower-resolution grids (e.g., 4–5 km), based on the findings of Fierro et al. (2009a). The runs have 55 vertical levels, with a higher vertical resolution in the planetary boundary layer (~19 levels below 850 hPa) and near the model top (10 hPa), following Kimball and Dougherty (2006) and Chen et al. (2011). The two outer nests use the Kain–Fritsch cumulus parameterization (Kain and Fritsch 1990; Kain 2004), but the inner nest does not use a cumulus parameterization. For both shortwave and longwave radiation the model uses the Rapid Radiative Transfer Model for GCMs (RRTMG) scheme (Iacono et al. 2008). The Yonsei University (YSU) planetary boundary layer (PBL) scheme is used (Noh et al. 2003; Hong et al. 2006), and a TC surface flux scheme is used to account for the changes in the drag and enthalpy coefficients at high wind speeds (Powell et al. 2003; Davis et al. 2008; Dudhia et al. 2008). The model makes use of the Morrison double-moment microphysics scheme (Morrison et al. 2005). Many of these parameterizations are similar to the schemes used in the "hurricane nature run" of Nolan et al. (2013).

### b. Selected TCs

The two cases (Dean in 2007 and Bill in 2009) were selected because they remained over the ocean for most of the period of interest, removing the complicating effects of land interaction. Hurricane Dean formed from an African easterly wave (AEW), moved into the Caribbean Sea as it rapidly intensified in a relatively low-shear environment

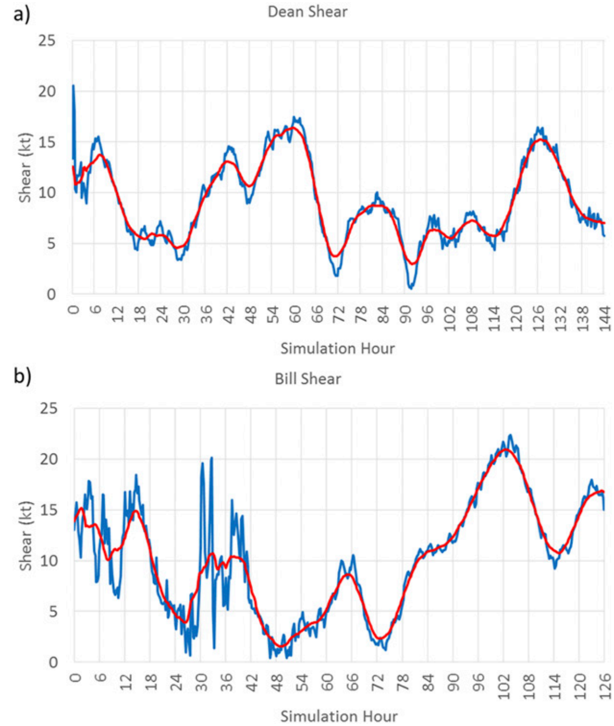


FIG. 1. Vertical shear time series for the (a) Dean and (b) Bill simulations. The blue line is the full time series of shear, and the red line shows a smoothed shear value calculated by a 6-h running average.

for most of its life (Fig. 1a), weakened as a result of an eyewall replacement cycle, and reintensified before landfall in the Yucatan Peninsula (Franklin 2008). Bill also formed from an AEW (Avila 2009), but recurved northeast of the Lesser Antilles because of a weakness in the subtropical ridge. It weakened as it moved into the north-central Atlantic, possibly because of the effects of increasing shear (Fig. 1b) and restricted outflow on the south and west sides of the TC. Both TCs experienced periods of steady intensification, rapid intensification, and weakening (Fig. 2), allowing for study of the relationship between CBs and intensity change. The two TCs provide an interesting comparison between one TC (Dean) that experienced few detrimental effects from environmental factors and experienced mostly internally driven intensity changes and another (Bill) that experienced a combination of internal changes as well as external forcing from shear and dry air. These differences are discussed below, and play a key role in the structure and evolution of the simulated CBs.

### c. WRF representations of the TCs

The simulation for Dean covered 144 h of the storm's life cycle, from 0000 UTC 15 August to 0000 UTC 21 August 2007. Figure 2a shows the track and intensity of the observed TC (from the National Hurricane Center's

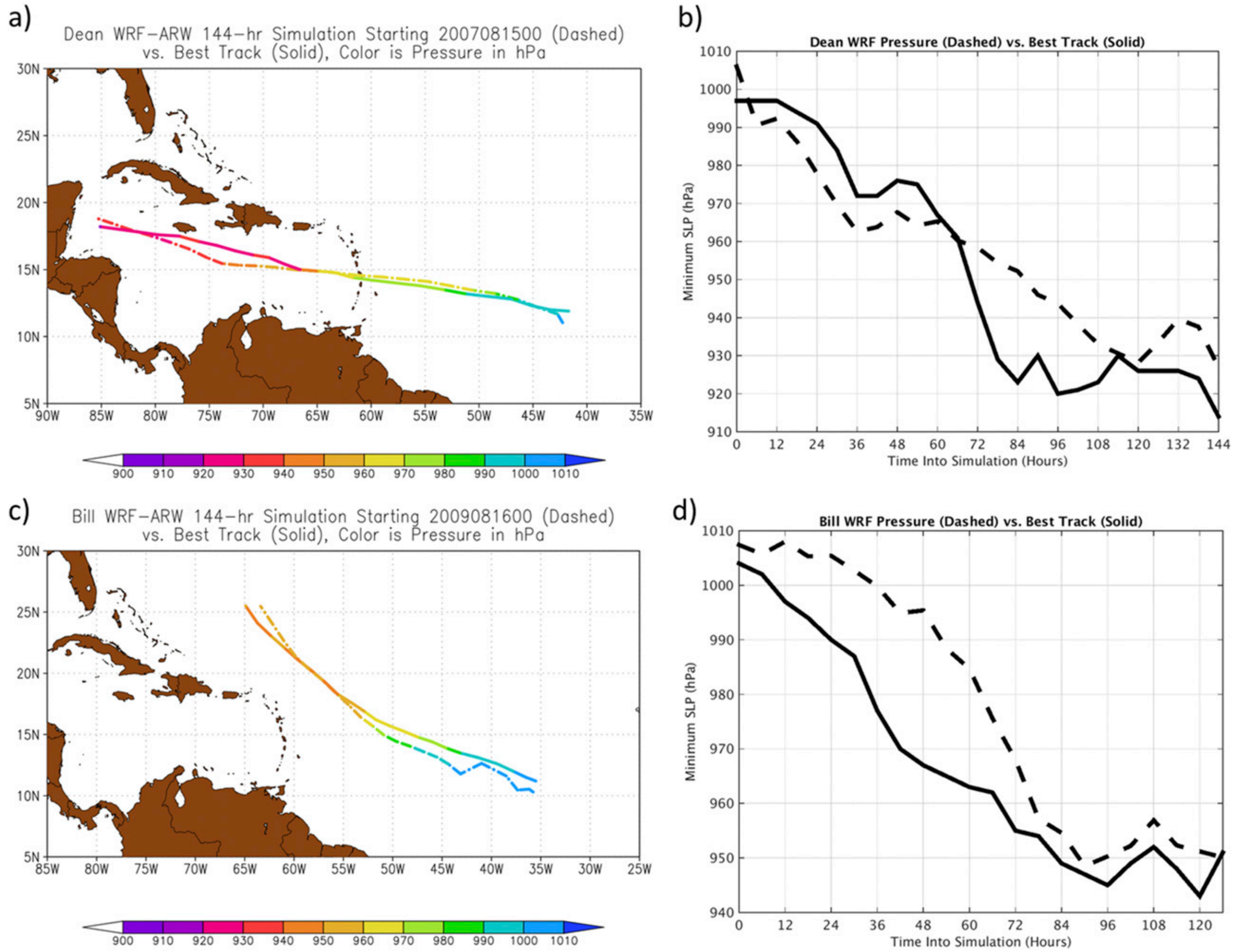


FIG. 2. (a) Tracks of Hurricane Dean (2007) from the best track dataset (solid) and the WRF simulation (dashed). The colors indicate the minimum central pressure of the observed and simulated TCs. (b) Intensities (minimum central pressure) of Hurricane Dean (2007) from the best track dataset (solid) and the WRF simulation (dashed). (c) As in (a), but for Hurricane Bill (2009). (d) As in (b), but for Hurricane Bill (2009).

best track dataset) and the simulation. For the length of the simulation, the track is well represented in the model, with only slight deviation toward the end of the period. With intensity, the first 60 h or so are well represented. Afterward, the model produces a period of intensification, although not as rapid as in the observations. Thus, there is some lag, but the model is able to come close to reproducing the peak intensity and also shows the weakening and reintensification in the observed TC.

The simulation for Bill covered 126 h, from 0000 UTC 16 August to 0600 UTC 21 August 2009. Figure 2b shows the track and intensity of the observed and simulated TCs. As with Dean, the model generally captures the track, especially after some initial oscillations during spinup. Similarly, although the intensification rate is slower than observed during the first 36 h, for the rest of the simulation the intensity change trends are well captured by the model. The model once again comes close to reproducing the maximum intensity. As will be seen in Part II, the model also reproduces some of the structural features seen in the observed TCs, although the eye tends to be too large. The reasons for this size bias are unclear, although it could be related to horizontal resolution (e.g., Davis et al. 2008), deficiencies in the simulation of eye–eyewall mixing, and/or unrealistic representation of boundary layer diffusivity (e.g., Zhang et al. 2015; Zhang and Marks 2015). In summary, although simulations cannot be perfect, they capture many of the salient features of the observed track and intensity.

## 3. Results

### a. Locations of CBs

CBs were identified by examining the distribution of eyewall vertical velocity. The methodology is similar to that used by Rogers et al. (2013), which defined CBs based on the 99th percentile of updraft vertical velocity at $z = 8$ km in airborne radar data. While it is possible that lower-level updrafts can play a role in structure and intensity change, that study found that the upper-level updrafts and higher percentiles of vertical velocity (i.e., >95th) showed a much stronger signal for intensity change, and these most extreme updrafts will be the focus of this paper. In this analysis, however, rather than the single-level definition, CBs were defined based on a 6–12-km layer-mean vertical velocity. This change was due to the fact that the height of the updraft maximum was observed to vary with time in the simulations. Fierro et al. (2015) similarly found that the maximum electrification in Hurricane Isaac was found between 6 and 10 km. Part II will discuss TC intensity change and CBs, and will show that the differences between intensifying and weakening/steady cases is most pronounced for the higher percentiles and above a height of $z = 6$ km. The CB threshold was the 99th percentile of the eyewall vertical velocity (updrafts only) in this 6–12-km layer mean, where the eyewall region is defined in a polar coordinate system normalized by the radius of maximum wind averaged in the 6–12-km layer ($\mathrm{RMW}_{6\text{–}12}$, $R^*_{6-12} = r/\mathrm{RMW}_{6\text{–}12}$) as $R^*_{6-12} = 0.75$–1.25 [similar to Rogers et al. (2013) but using $z = 6$–12 km]. Throughout the study, $R^*_z = r/\mathrm{RMW}_z$ will be used to refer to the normalized RMW at a specific height $z$ in kilometers. Most figures will use $R^*_3$, although a few plots will use $R^*_{6-12}$. The center was not recalculated with height, so any effects from vortex tilt will be included. The normalization based on the RMW averaged over a layer (rather than at the bottom of the layer) was chosen because of the slope of the RMW (e.g., Stern and Nolan 2009; Stern et al. 2014; Hazelton and Hart 2013; Hazelton et al. 2015). This local RMW defines the boundary between the low inertial stability outside the RMW and the high inertial stability inside, where more latent heating from convection contributes to net warming (e.g., Schubert and Hack 1982; Nolan et al. 2007; Vigh and Schubert 2009). The CB threshold here for the Dean simulation was $8.4\,\mathrm{m\,s^{-1}}$, and for the Bill simulation it was $5.4\,\mathrm{m\,s^{-1}}$. The slightly weaker vertical velocity for Bill was likely due to the combination of a weaker TC (and associated secondary circulation) and a track over comparatively cooler sea surface temperatures (SSTs).[1]

Figure 3 shows the distribution of CBs relative to $\mathrm{RMW}_{6\text{–}12}$ and the shear direction for both simulations. The four shear-relative quadrants are defined/labeled as follows: downshear left, DSL; downshear right, DSR; upshear left, USL; and upshear right, USR. The CB locations were calculated in a normalized radius–azimuth coordinate system, and interpolated to a Cartesian coordinate system for the density plots, also normalized by $\mathrm{RMW}_{6\text{–}12}$. The density is binned every $0.1X/\mathrm{RMW}_{6\text{–}12} \times 0.1Y/\mathrm{RMW}_{6\text{–}12}$, such that the diagrams are essentially a two-dimensional histogram showing CB counts. The counts are normalized by the sample size (number of 15-min output times) in each case. As can be seen from the figures, the density of the CBs is much higher inside $\mathrm{RMW}_{6\text{–}12}$ than outside, although CBs can be found well outside the eyewall region. These distributions are generally consistent with the climatology of Tao and Jiang (2013), which found that the occurrence of TC hot towers was more common closer to the TC center (where convective precipitation was dominant) than the outer rainbands. For both TC simulations, the highest concentration/number of CBs is in the downshear region, particularly DSL, consistent with previous observational studies (e.g., Black et al. 2002; Rogers et al. 2013; Reasor et al. 2013; D14). This distribution is especially pronounced outside the RMW for the Bill simulation, likely because of higher shear, especially later in its life cycle (Fig. 1).

### b. Composites of CB and non-CB locations

The fact that CBs in the simulations tend to develop in the shear-relative regions consistent with observations and theory (cf. Fig. 3) indicates that the structural changes to the vortex caused by vertical shear can provide a preferential azimuthal location for CB development. We next begin to examine some of the factors influencing CB development in more detail, first through composites of locations with CBs inside $\mathrm{RMW}_{6\text{–}12}$ and locations with no CBs. This was done by determining whether there was at least one CB anywhere in the radial direction (at an azimuthal resolution of 5°) for a given azimuth. If there was at least one CB in the radial, and this CB was inside $\mathrm{RMW}_{6\text{–}12}$ (at that azimuth), this radial was included in the CB composites. If there were no CBs anywhere in the radial, this radial was included in the non-CB composites. It should be noted that this 5° azimuthal resolution will lead to different areas covered in each interpolated grid cell at different radii, which may have caused a few CBs to be "smoothed out" in a particular composite, especially in the outer region of the TC. Most CBs included multiple azimuths meeting the threshold value, and so most CB composites include azimuthal variation. However, some

[1] Although this methodology produces different values for the two TCs, it eliminates differences simply due to TC environment (specifically SST or outflow temperature) and allows for study of the impact of TC structure on CBs.

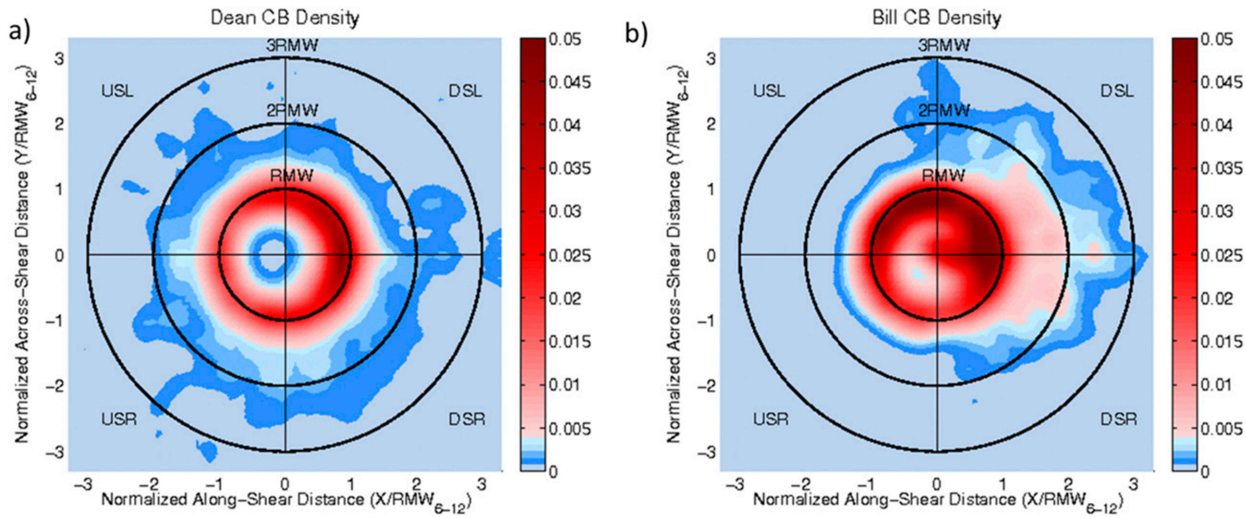


FIG. 3. (a) Density (count per normalized 0.1 × 0.1 grid point, per simulation hour) of convective bursts in the Dean simulation (calculated by binning all of the CBs from Dean after spinup). The horizontal coordinate system is normalized by the 6–12-km mean RMW, and also rotated relative to the 850–200-hPa shear vector. The counts are normalized by the number of cases in each simulation. (b) As in (a), but for the Bill simulation.

of the CB forcing may occur at azimuths upwind from the CBs, and this full three-dimensional evolution is explored later in our trajectory analysis.

If there was a CB along the radial, but only outside $RMW_{6–12}$, this radial was not included in either composite. The composite of CBs outside the RMW (not shown) had a similar structure near the RMW to the non-CB composite. For the composites, the radial coordinate system was normalized by the 3-km RMW ($R_3^* = r/RMW_3$), near the height of most reconnaissance flights and similar to composite radar studies (e.g., Rogers et al. 2013; Reasor et al. 2013; D14), to allow for compositing of times with different eye sizes. As will be shown in a later paper, there were periods of enhanced and reduced CB activity at many different intensities throughout the life cycle of each storm, so the different structures seen in the composites are likely not solely a result of intensity differences. It is also worth noting that this analysis also does not remove the effects of shear, which means that the asymmetries in the composites are likely a combination of shear-induced asymmetries and their impact on convection as well as higher-order asymmetries.

Figure 4 shows the radial velocity for the CB and non-CB radials. The low-level (0–1 km) inflow is stronger (composite mean $\sim$20 m s$^{-1}$) for the CB locations, and there is also weak inflow over a much deeper layer: up to $\sim$9 km in the CB composite, but only $\sim$6 km in the non-CB composite, implying the possibility for deeper-layer convergence. Another key feature seen at 2–4-km height is the strong outflow ($\sim$10–15 m s$^{-1}$) radially inward of the RMW in the CB composite. This feature is much weaker in the non-CB composite. It is likely related to supergradient flow above the boundary layer from inflowing parcels that overshoot the RMW (e.g., Shea and Gray 1973; Smith et al. 2009), and may also be indicative of eye–eyewall exchanges in some instances (e.g., Braun 2002; Eastin et al. 2005). Coupled with the stronger radial inflow, this suggests stronger radial convergence in the CB composite. Both of these points will be examined in more detail later.

At upper levels, additional differences are noted. There is stronger outflow aloft in the CB composite than in the non-CB composite, and the outflow is maximized closer to the updraft in the CB composite. A similar combination of stronger inflow at low levels and stronger outflow aloft was noted by D14 in shear-relative Doppler radar composite comparisons of strong updraft versus strong downdraft locations. This radial flow difference may be due to burst structure as well as shear-relative flow, with the non-CB locations representing the background secondary circulation and the CB composites showing perturbations due to forcing on different scales. Finally, a region of inflow inside the RMW is apparent in the radial flow of the CB composites (especially for Dean), but the same feature is weaker/nonexistent in the non-CB composites, implying that the CBs potentially contribute significantly to the compensating subsidence in the eye, which can lead to pressure falls in the core (e.g., Heymsfield et al. 2001; Guimond et al. 2010).

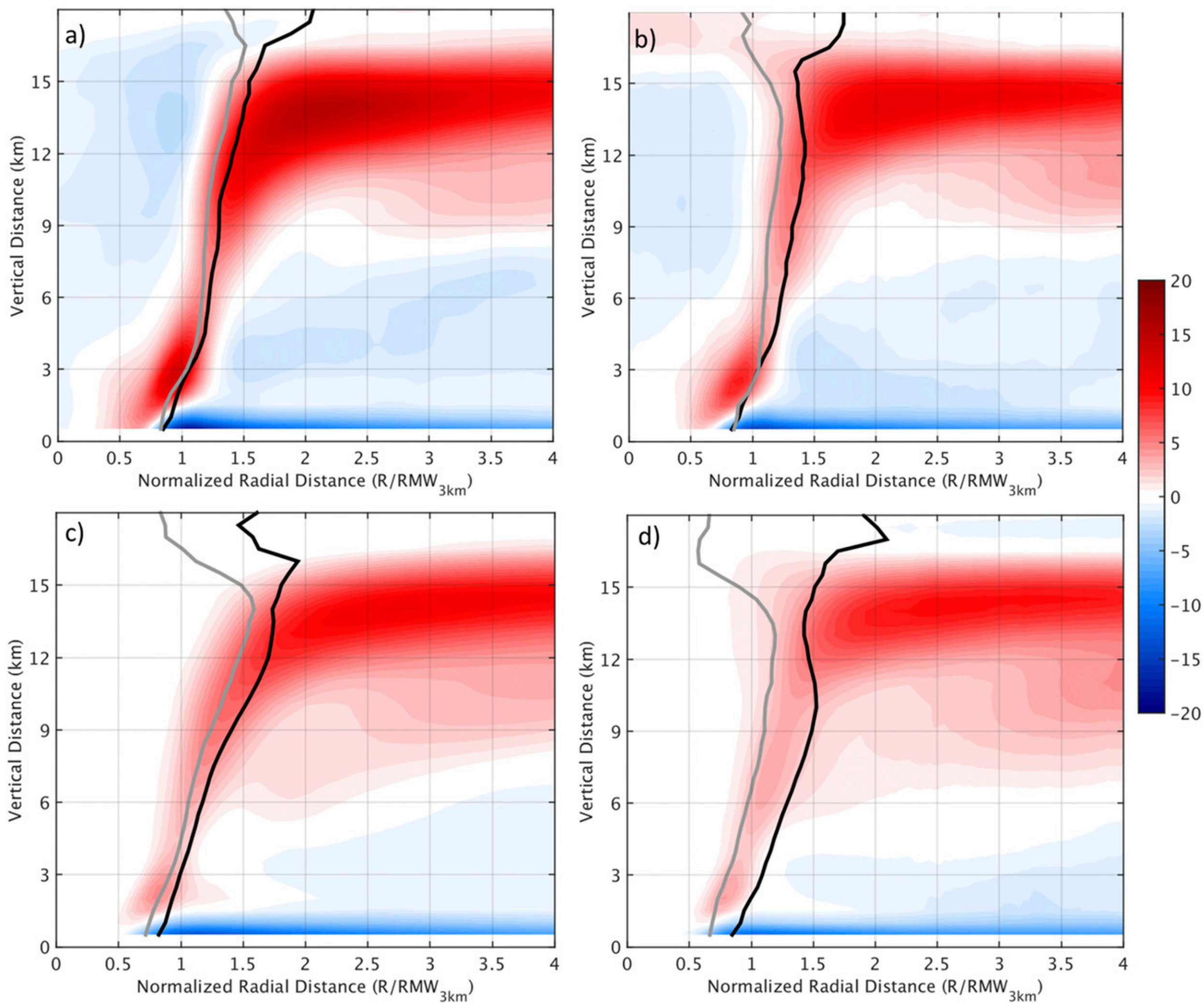


FIG. 4. Azimuthal composites of radial velocity (m s$^{-1}$) for (a) azimuths in the Dean simulation with at least one CB inside the RMW. The solid black line is the composite mean RMW and the solid gray line is the composite mean updraft core. (b) As in (a), but for the Bill simulation. (c) As in (a), but for the azimuths in the Dean simulation with no CBs. (d) As in (c), but for the Bill simulation.

### *c. Radial convergence and CB locations*

Since the composite results imply that enhanced lower-level convergence may be one of the key forcing mechanisms for CBs, individual time periods are examined next to investigate the importance of radial convergence in controlling the radial locations of CBs with respect to the RMW at lower levels ($\mathrm{RMW}_1$) and above ($\mathrm{RMW}_{6\text{–}12}$). Radial divergence is calculated by

$$\mathrm{Divergence}_{\mathrm{radial}} = \frac{\partial u_r}{\partial r} + \frac{u_r}{r}. \qquad (3.1)$$

Figure 5 shows radial divergence as well as the total divergence (which includes an azimuthal component) at $z = 1$ km and CB locations at two contrasting times: hours 67.25 and 97.25 of the Bill simulation. Based on these two values, the radial convergence appears to be the dominant component of convergence. At hour 67.25, the CBs are close to the radial convergence in the eyewall. Although the CBs are outside $\mathrm{RMW}_1$ as a result of the slope of the eyewall, they appear to be inside the RMW at upper levels. This slope of the eyewall also explains why the CBs are found radially outward from the low-level convergence. For hour 97.25, the CBs appear both in the eyewall radially outward from a convergence maximum as well as in an outer band in the downshear region with a pronounced convergence maximum. These CBs in the outer band are well outside both $\mathrm{RMW}_1$ and $\mathrm{RMW}_{6\text{–}12}$. The area of convergence in the downshear region is associated with a developing updraft that becomes a CB 15–30 min later (not shown).

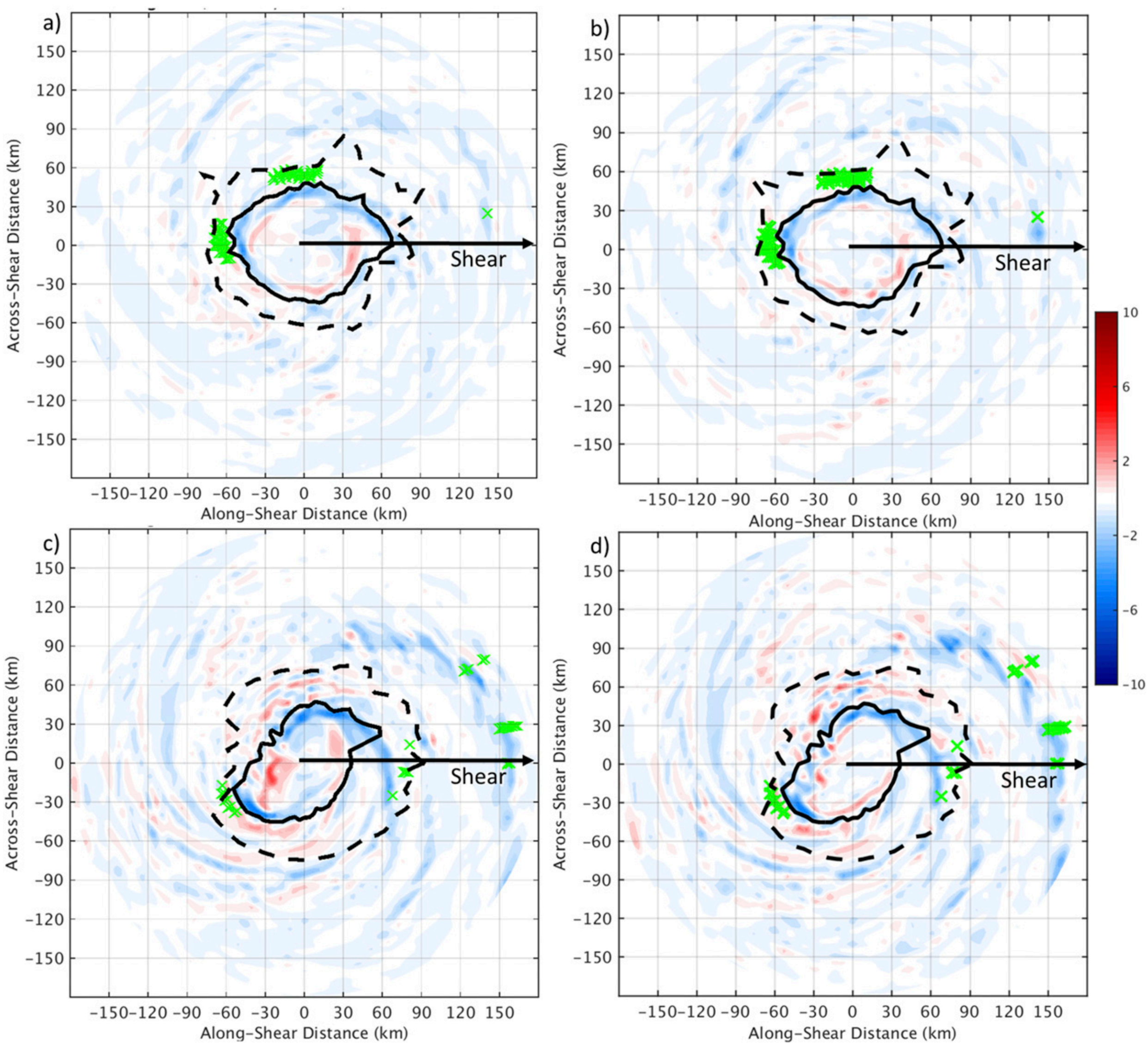


FIG. 5. (a) Radial divergence ($10^{-3}\,s^{-1}$) at $z = 1$ km and CB locations (green crosses) at hour 67.25 of the Bill simulation. (b) Total divergence ($10^{-3}\,s^{-1}$) at $z = 1$ km and CB locations (green crosses) at hour 67.25 of the Bill simulation. (c) As in (a), but for hour 97.25 of the Bill simulation. (d) As in (b), but for hour 97.25 of the Bill simulation. In all panels, the solid black line is the RMW at $z = 1$ km and the dashed black line is the $z = 6$–12-km mean RMW. The coordinate system is rotated relative to the shear vector.

To examine further the connection between convergence and CBs, the low-level convergence was correlated with CB counts in normalized radial bands, from 0.5 to 2.5 $RMW_3$ in 0.25-RMW increments. The results (Table 1) show statistically significant positive correlations in all bands. The peak in correlation is found near the eyewall, with a secondary peak radially outward, perhaps near the location of prominent bands or secondary eyewalls. These examples seem to indicate that the location of low-level radial convergence can indeed play a role in governing the radial distribution of the CBs. However, it should also be noted that the strong convergence could also be a response to the developing updraft, leading to a feedback process.

### d. Asymmetric vorticity and CB development

Based on the composite results and analysis of radial convergence, anomalous radial flow appears to be a forcing mechanism for CBs. In this section, one of the possible factors influencing radial flow is explored: asymmetric vorticity. As mentioned previously, studies (e.g., Braun et al. 2006; Guimond et al. 2016) have linked eyewall convection to mesovortices. Here, we explore whether asymmetric vorticity is connected to the most extreme TC updrafts.

TABLE 1. Correlation between low-level convergence in different radial bands (normalized by the 3-km RMW) and CB counts in each band for each of the two simulated TCs. The correlations significant at the 95% confidence level are italicized, and those significant at the 99% level are set in boldface.

| TC | 0.5–0.75 × $RMW_3$ | 0.75–1.0 × $RMW_3$ | 1.0–1.25 × $RMW_3$ | 1.25–1.5 × $RMW_3$ | 1.5–1.75 × $RMW_3$ | 1.75–2.0 × $RMW_3$ | 2.0–2.25 × $RMW_3$ | 2.25–2.5 × $RMW_3$ |
|---|---|---|---|---|---|---|---|---|
| Dean | 0.08 | **0.27** | **0.43** | **0.34** | **0.23** | **0.14** | **0.26** | **0.25** |
| Bill | **0.30** | **0.18** | **0.29** | **0.56** | *0.11* | **0.27** | **0.16** | **0.24** |

The asymmetry in vorticity was quantified by examining the azimuthal standard deviation of vorticity at $z = 2$ km, calculated along $RMW_2$ every 5° azimuthally:

$$\zeta_{\text{variance}} = \sigma_{0-360}(\zeta_{2\text{km}}). \tag{3.2}$$

This metric (where a higher variance indicates a more asymmetric eyewall) was correlated with CB count inside the RMW, and shows statistically significant correlation with CB count for Dean ($r = 0.43$, $p < 0.01$). However, this relationship is much weaker and of the opposite sign ($r = -0.15$, $p < 0.01$) for the Bill simulation. This relationship seems to indicate that for Dean, the asymmetric vorticity (often wavenumber 2 or higher, as will be shown) was a relatively significant factor in governing the locations of the CBs, through low-level convergence and also injecting parcels into the eyewall. However, for Bill, this asymmetric vorticity did not appear to play as large of a role, potentially because of the higher shear inducing more of a steady azimuthal variance as a result of a wavenumber-1 asymmetry. This result is consistent with a simulation of Hurricane Erin by Braun and Wu (2007), which found that a wavenumber-1 asymmetry in vertical motion dominated in times of high shear and that vertical motion was driven more by small-scale features (such as mesovortices) in low-shear environments.

Despite the overall weak relationship in Bill, individual time periods within the Bill simulation did appear to show some connection between mesovortices and CBs. However, since Dean showed the stronger relationship, the relationship between mesovortices and CBs is next explored for a key time period in that simulation. Figure 6 shows the following variables at $z = 2$ km from hours 96 to 101 of the Dean simulation: azimuthal anomaly of vorticity, azimuthal anomaly of divergence (at a threshold value of $5 \times 10^{-3}\,\mathrm{s}^{-1}$), and the asymmetric wind field. CB locations were also overlaid. Both the asymmetric vorticity and asymmetric wind are calculated by subtracting the azimuthal mean at each radius from the full fields. Early in this period, the CBs are mainly concentrated in the DSL region, with a few CBs right of shear. Around hours 98 and 99 the eyewall becomes more asymmetric, and a wavenumber-2 pattern develops, with CBs associated with the mesovortices even in the USL and USR regions of the TC. At hour 101, one of the mesovortices does not seem to be associated with CBs, but this was found to be a growing updraft that was below the 6–12-km threshold at this time (not shown), and reached 6 km later. The asymmetric convergence shows that the CBs tend to form radially outward of low-level convergence, although not all convergence leads to CBs; the convergence associated with asymmetric low-level outflow seems to be much more associated with CBs than the convergence with asymmetric inflow. Although only one case, this result indicates that the asymmetric dynamics associated with eyewall breakdown may allow strong convection to develop and persist upshear (USL/USR), as well as allowing the mesovortices to grow through vorticity stretching. The asymmetric cyclonic flow associated with the mesovortices promotes outflow from the eye to the eyewall, adding to the typical outflow due to supergradient flow above the boundary layer as well as inertial overshooting of inflowing parcels inside the RMW, creating convergence in a background of inflow.

### e. Analysis of individual CBs

The evolution of the radial flow and its relationship to CB formation was analyzed by tracking individual CBs rotating around the eyewall. The CBs were tracked by finding the azimuth of the maximum 6–12-km vertical velocity within the region meeting the CB threshold. The vertical and radial velocities were assessed as the CBs rotated around the eyewall. Four individual CBs were tracked: two each for Dean and Bill. The CBs were tracked from an hour before to an hour after the maximum in vertical velocity.

An example of the vertical velocity following one of the Dean CBs is shown in Fig. 7. This period corresponds approximately to that analyzed in Figs. 6c–e from hours 97.75 to 99.75. The vertical velocity intensifies after the burst rotates from the DSR quadrant into the DSL, and peaks in the USL. This is slightly different than convective maximum in the DSL quadrant seen in other studies (e.g., Braun et al. 2006; Reasor et al. 2013), perhaps because of the analysis here being done at upper levels. Also, as the previous section shows, the

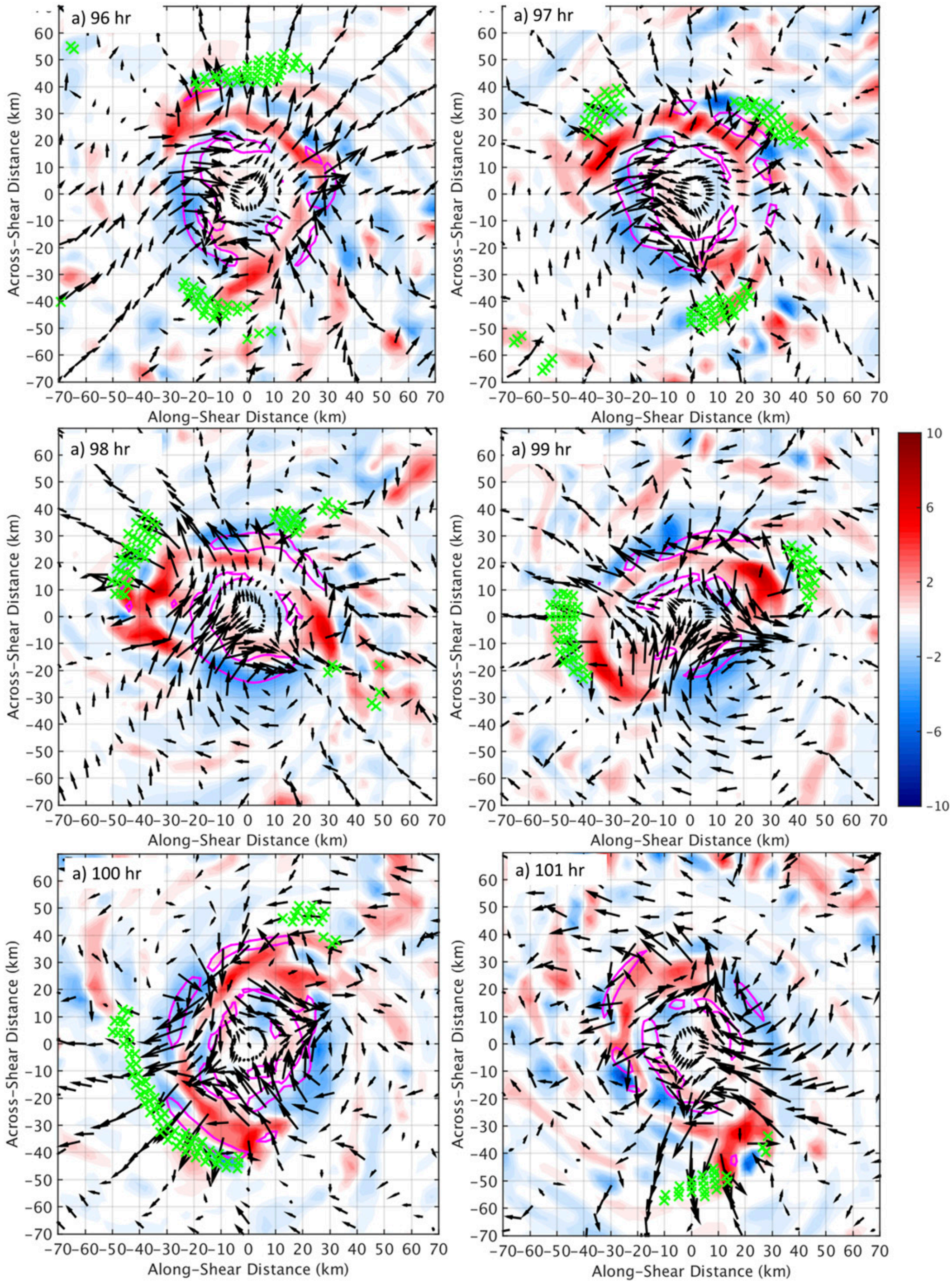


FIG. 6. The 2-km azimuthal vorticity anomaly ($10^{-3}\,s^{-1}$, shaded), azimuthal divergence anomaly ($-5 \times 10^{-3}$ contoured in magenta), azimuthally asymmetric wind vectors, and CB locations (green crosses) for the following numbers of simulation hours of the Dean simulation: (a) 96.0, (b) 97.0, (c) 98.0, (d) 99.0, (e) 100.0, and (f) 101.0. The coordinate system is rotated relative to the shear vector.

mesovortices, rather than vertical shear, appeared to be the dominant forcing during this time. The updrafts may have also begun to grow at lower levels in the DSL quadrant before reaching their 6–12-km peak in the USL (e.g., Halverson et al. 2006). The burst does weaken as it moves farther upshear, however, consistent with the evolution of updrafts in Braun et al. (2006) and Braun and Wu (2007).

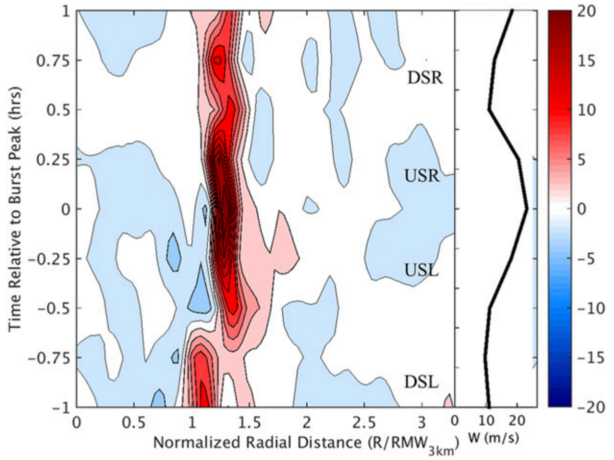


FIG. 7. Dean simulation Hovmöller diagram of 6–12-km mean vertical velocity (m s$^{-1}$) as a function of normalized radial distance for the CB peaking at hour 98.75 of the simulation. The time is plotted relative to the peak of the CB. The line plot on the far right shows the vertical velocity of the CB at each time. The shear-relative quadrants that the CB entered at different times relative to the peak are labeled on the right side of the graph.

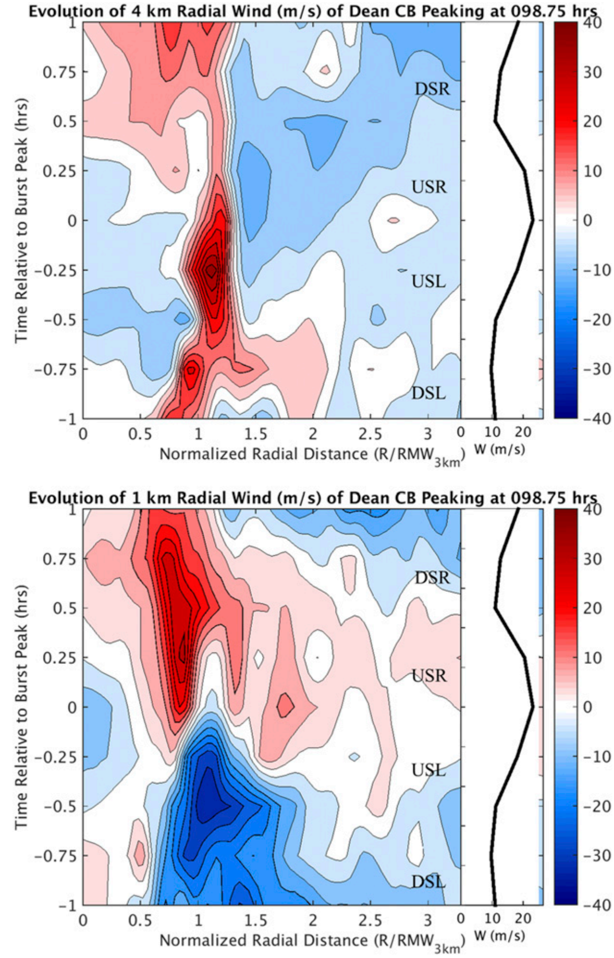


FIG. 8. Dean simulation Hovmöller diagram of radial velocity (m s$^{-1}$) at $z$ = (a) 4 and (b) 1 km as a function of normalized radial distance for the CB peaking at hour 120.25 of the simulation. The time is plotted relative to the peak of the CB. The line plot on the far right shows the vertical velocity of the CB at each time. The shear-relative quadrants that the CB entered at different times relative to the peak are labeled on the right side of the graph.

Figure 8 shows the radial velocity at two heights ($z$ = 1 km in the inflow layer and $z$ = 4 km, toward the top of the low-level outflow) following this same CB before and after the maximum vertical velocity. The low-level inflow at $z$ = 1 km peaks prior to the maximum in CB vertical velocity at upper levels, and the 4-km outflow also peaks prior to the updraft peak. The 4-km outflow drops off quickly as the CB decays, and the PBL inflow also weakens as the CB rotates into the upshear region and weakens. The change from low-level inflow to outflow in the upshear region is consistent with the composite results of Reasor et al. (2013). This evolution of the radial flow structure provides further evidence of the importance of strong low-level inflow and supergradient outflow from the eye to the eyewall (e.g., Shea and Gray 1973; Smith et al. 2009) in CB development.

To compare the previous CB with a case from the Bill simulation, Fig. 9 shows the Hovmöller diagram of the vertical velocity following one of the Bill CBs, from hours 111.75 to 113.75. Although the maximum vertical velocity is weaker and the CB progresses more slowly (because of weaker tangential wind in Bill), the evolution of the vertical velocity is similar. The burst grows within the DSL quadrant, peaks shortly after entering the USL quadrant, then weakens as it rotates farther upshear. Thus, although the composites showed more of a downshear preference for CBs in Bill (see Fig. 3b), the higher-wavenumber dynamical forcing allowed them to occasionally grow upshear. Figure 10 shows the radial velocity following this CB. Once again, there is strong low-level inflow in the DSL quadrant and partially in the USL quadrant as the burst grows, which switches to outflow farther upshear as the CB decays. The fact that this low-level outflow peaks during the CB decay stage indicates that outflow near this particular height is likely not important in CB development. At 4 km, the outflow from the eye to the eyewall again peaks prior to the maximum vertical velocity. In this case the midlevel inflow is also stronger prior to the CB peak. This timing indicates radial flow forcing the CBs, although the timing could be partially due to identifying CBs aloft while the radial flow anomalies are at lower levels.

This analysis was performed for four different cases (two in each TC, two of which are not shown but had

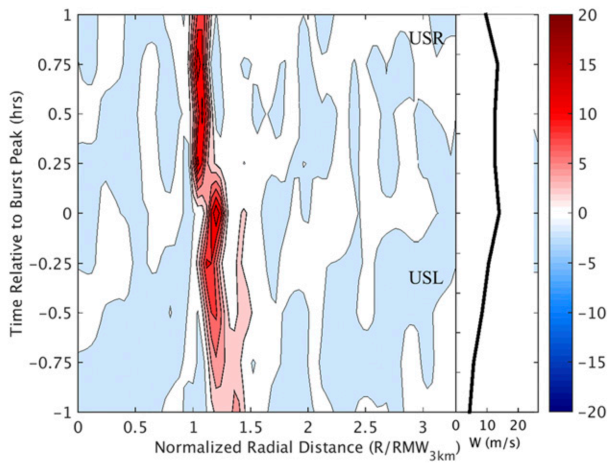


FIG. 9. As in Fig. 7, but for the CB peaking at hour 112.75 of the Bill simulation.

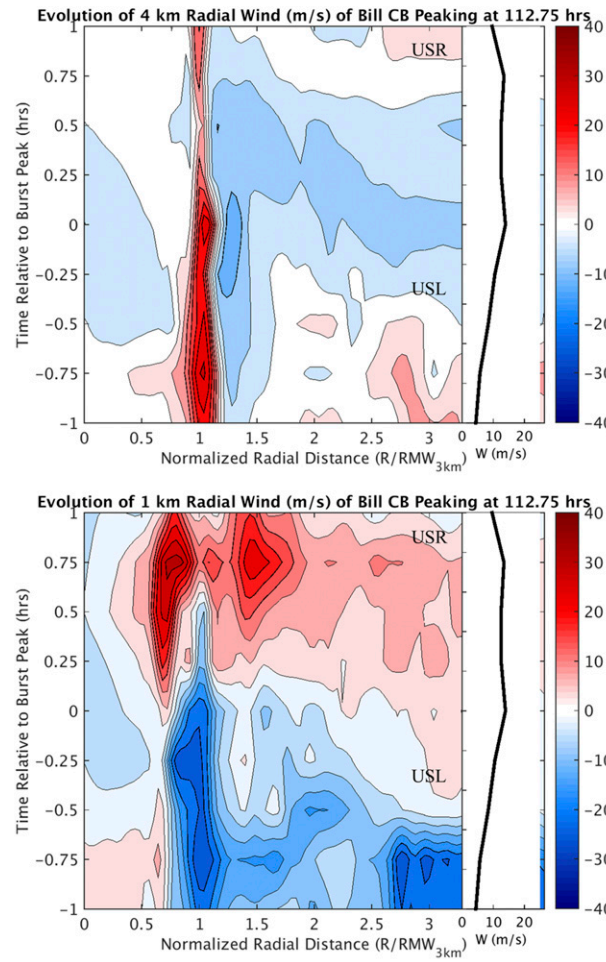


FIG. 10. As in Fig. 8, but for the CB peaking at hour 112.75 of the Bill simulation.

similar results), and the results were averaged. To show the full vertical extent of the differences in radial flow structure between growing and decaying CBs, Fig. 11 compares the $r$–$z$ mean of the CB radial flow in the time period (covering 1 h) while the CBs are intensifying versus hour when they are weakening. Several differences in radial flow structure stand out. In particular, the intensifying CB mean exhibits strong low-level inflow well inside the RMW, while the weakening CBs average show inflow that is weaker and does not extend inside $R_3^* = 1$. In addition, the low-level inflow in the intensifying CBs is deeper, extending up to about $z = 2$ km, while for the weakening CBs it is confined to the lowest $\sim$500–1000 m. This pattern is indicative of stronger radial convergence inside the RMW for the intensifying CBs, with convergence farther outward for decaying CBs.

Above 9 km, the weakening CBs have slightly stronger outflow aloft but the radial inflow back into the eye is only present for the intensifying CBs. This structural difference has implications for TC intensification. This inflow is part of the circulation with forced subsidence into the eye on the inward side of the CBs, which has been hypothesized as a mechanism for warming of the eye (Guimond et al. 2010; Chen and Zhang 2013; Chen and Gopalakrishnan 2015). It appears from these averages that this structure is more prevalent in CBs that are growing. The stronger outflow for the decaying CBs is likely a reflection of the air exiting the eyewall at upper levels after the maximum in vertical velocity, although some of the upper-level outflow is found downwind of the peak in vertical velocity below (not shown).

Overall, the mean radial flow structures for the intensifying CBs are generally consistent with the quadrant-based composites of intense updrafts in D14, which revealed stronger low-level inflow and upper-level divergence DSL, with weak low-level outflow and less upper-level divergence upshear. CB development is favored in the downshear region where low-level inflow is dominant, and also in regions where mesovortices lead to stronger radial convergence and exchange of air between the eye and eyewall. As has been mentioned previously, it is also possible that some of the radial flow anomalies occur as a result of the radial wind responding to the developing updraft at upper levels, such that these processes can be seen as a feedback. However, the timing suggests that the radial flow is an important forcing mechanism preceding the peak in vertical velocity. Next, the connection of the radial flow anomalies to potential eye–eyewall mixing is explored.

### *f. Outflow from the eye to the eyewall*

To determine whether the outflow-seen composites is coming from the eye (indicative of eye–eyewall exchange) or simply moving outward in the eyewall updraft,

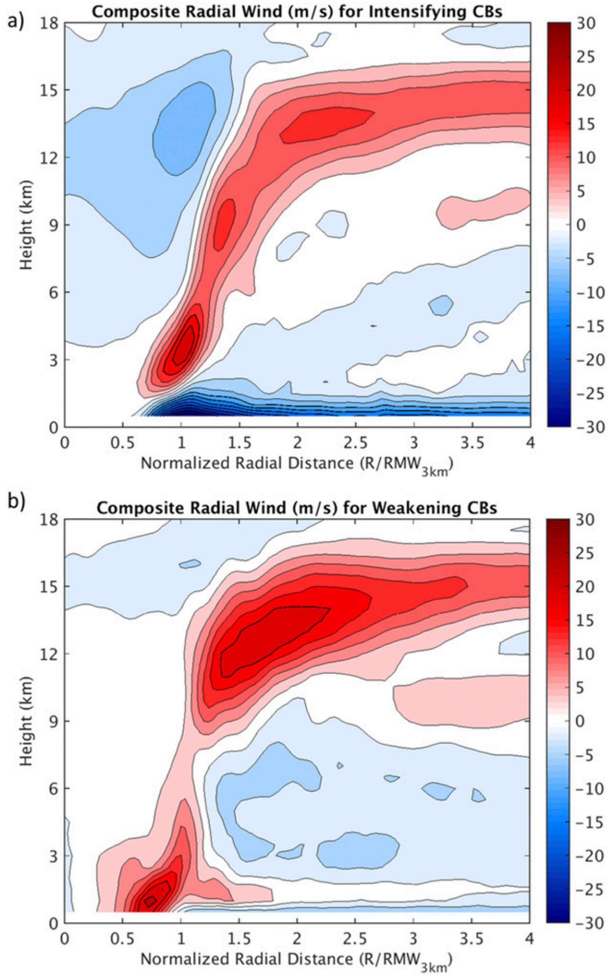


FIG. 11. Mean radial velocity from the four tracked CBs for (a) hours −1 to −0.25 prior to the CB peak, when the CB was intensifying, and (b) hours 0.25 to 1 after the CB peak, when the CB was weakening.

two of the CBs from the previous section are analyzed in further detail: the CB peaking at hour 98.75 of the Dean simulation and the CB peaking at hour 112.75 of the Bill simulation. These CBs will later be analyzed in three-dimensional detail via trajectory analysis. Figure 12 shows several variables at $z = 2$ km for each case 15 min prior to the updraft peak, at hour 98.50 of the Dean simulation and hour 112.50 of the Bill simulation. The variables shown are the reflectivity $\theta_e$ [calculated according to Bolton (1980)] and vorticity. Also overlaid on each plot are the asymmetric flow vectors (e.g., Fig. 6) and the 6–12-km vertical velocity meeting the CB threshold. The gray hatching in each figure shows the release points of three-dimensional trajectories (see next section).

The vorticity plots (Figs. 12a,b) show that the anomalous outflow for these two cases seems to be associated with mesovortices, as was shown in Fig. 6. The reflectivity plots (Figs. 12c,d) reveal that much of the anomalous outflow begins within the low-reflectivity area inside the eye and then extends into the eyewall. Consistent with this notion, the plots of $\theta_e$ (Figs. 12e,f) also show that much of the anomalous outflow comes from the high-$\theta_e$ air within the eye, indicative of mixing of this high-$\theta_e$ air between the eye and the eyewall. As further evidence of this mixing, the $\theta_e$ plot for Dean especially shows an extension of the warm core into the eyewall near the CB, and extending downwind. Such a ''warm-core protrusion'' was seen at $z = 2$ km in a study of Hurricane Karl by Guimond et al. (2016) and was found to be associated with intense convection. Thus, in both observations as well as the simulations shown here, the outflow from the eye to the eyewall appears to help mix high-$\theta_e$ air into the eyewall and aid in CB development. The next section explores the three-dimensional flow associated with these CBs to explore these mechanisms further.

### *g. CB trajectory analysis*

To analyze the three-dimensional nature of the radial flow anomalies that lead to CB formation, three-dimensional trajectories near CBs were calculated using the Hybrid Single-Particle Lagrangian Integrated Trajectory (HYSPLIT) model (Draxler and Hess 1997, 1998), and were calculated both forward and backward in time from the locations of interest. To determine the representativeness of a given trajectory, ensemble ''clusters'' of several trajectories with slight variations in initial horizontal and vertical positions were included, as will be discussed later in the section. The two particular cases analyzed were the individual CBs discussed in the previous section: hour 98.75 of the Dean simulation and hour 112.75 of the Bill simulation.

#### 1) TRAJECTORY INITIATION AND PATHS

The gray hatching in Fig. 12 shows the trajectory release points overlaid on the 2-km vorticity, reflectivity, and $\theta_e$. The trajectories were initiated near regions of strongly positive asymmetric vorticity, on the upwind (relative to the TC tangential winds) side of the mesovortex. The trajectories were calculated forward and backward 1 h from these points, at heights of 0.5–4 km. The trajectories were started 15 min before the peak in CB vertical velocity, to analyze the evolution of radial and vertical flows near the CB. A total of 968 trajectories were calculated for each case (11 × 11, every 0.02° horizontally, over eight vertical levels). For clarity of plotting, only the trajectory from each initiation height with the maximum vertical velocity in the updraft portion of the trajectory is plotted in Figs. 13 and 14 (eight trajectories total).

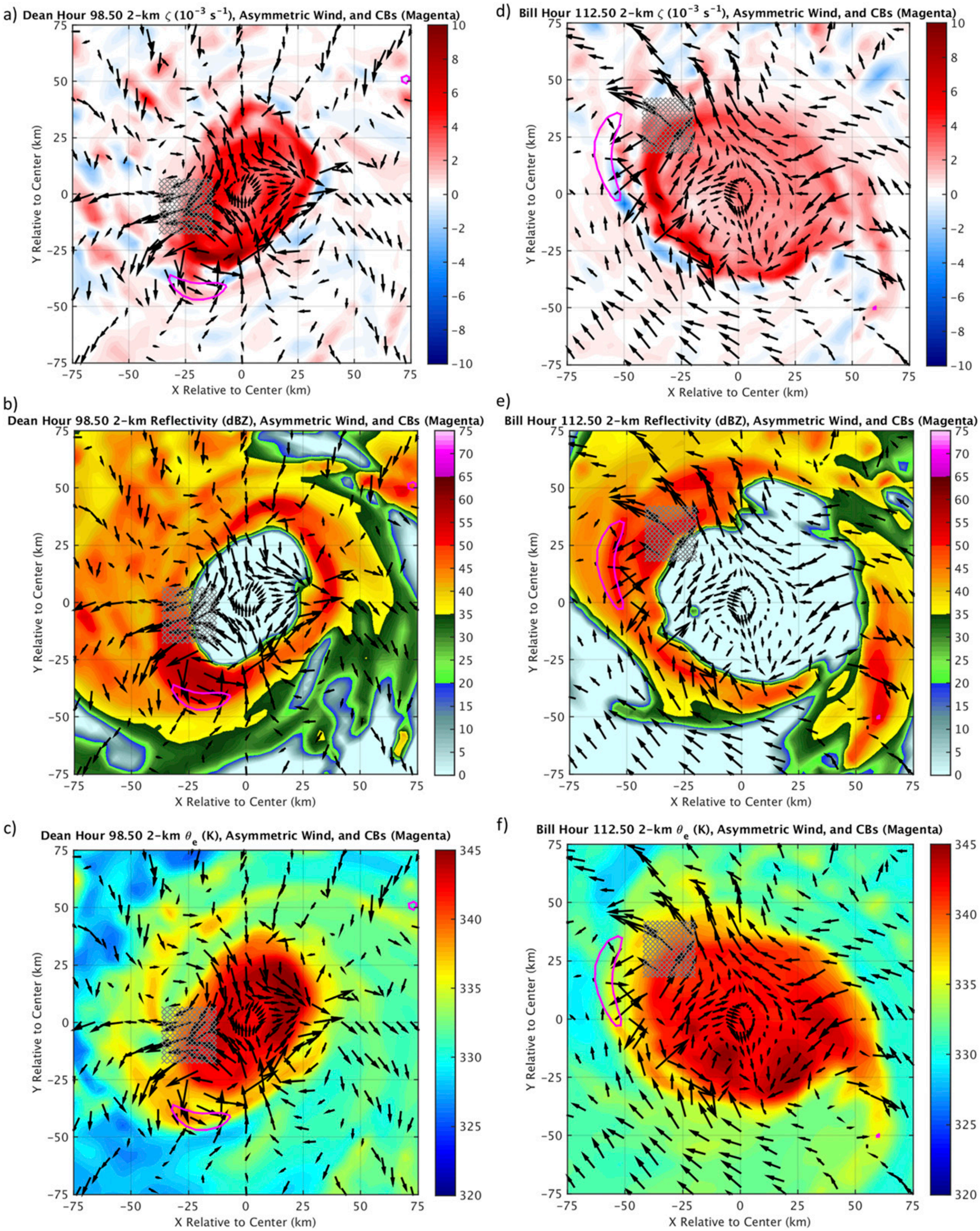


FIG. 12. (a) Vorticity at $z = 2$ km ($s^{-1}$, shading), azimuthally asymmetric wind vectors, 6–12-km mean vertical velocity meeting the CB threshold (magenta contours), and horizontal locations of trajectory release points (section 3g) at hour 98.50 of the Dean simulation. (d) As in (a), but for hour 112.50 of the Bill simulation. (b) As in (a), but the shading is reflectivity (dB$Z$) at $z = 2$ km. (e) As in (b), but for hour 112.50 of the Bill simulation. (c) As in (a), but the shading is $\theta_e$ (K) at $z = 2$ km. (f) As in (c), but for hour 112.50 of the Bill simulation.

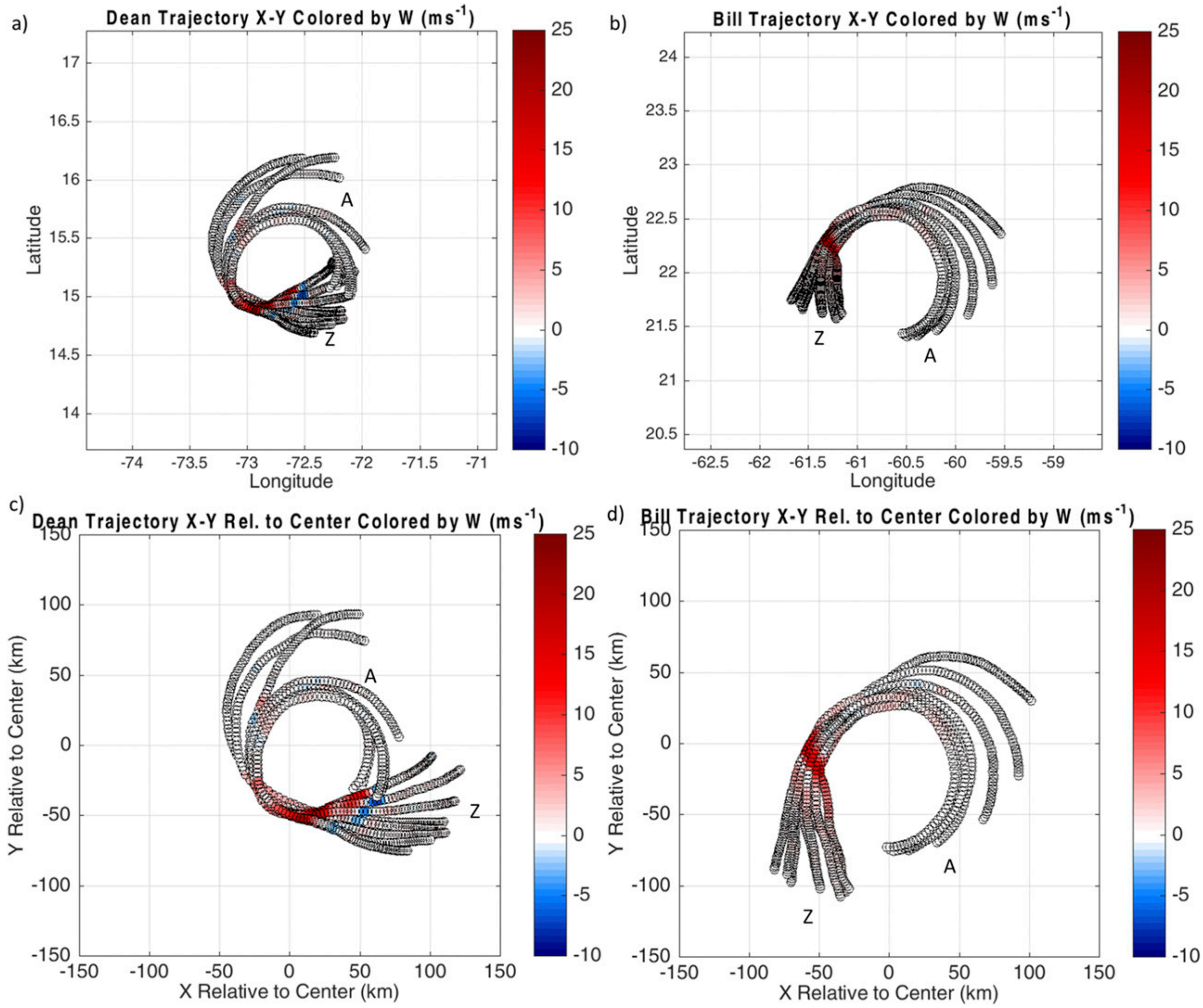


FIG. 13. (a) Paths of eight parcels (the parcel at each initiation height reaching maximum vertical velocity) in Earth-relative $X$–$Y$ space calculated forward 1 h and backward 1 h, centered at hour 98.50 of the Dean simulation. The letter A marks the start of the trajectories and the Z marks the end. The trajectory paths are shaded by the vertical velocity (m s$^{-1}$). (b) As in (a), but for hour 112.50 of the Bill simulation. (c) As in (a), but here the trajectories are plotted in a storm-relative coordinate system. (d) As in (c), but for hour 112.50 of the Bill simulation.

Figure 13 shows the $x$–$y$ paths of the eight maximum-$W$ parcels for each case and Fig. 14 shows the $r$–$z$ paths of the eight parcels for each case. The shading shows the vertical velocity, and shows that several of the Dean trajectories reach over 20 m s$^{-1}$ while several of the Bill trajectories reach 10–15 m s$^{-1}$, indicating they were indeed part of the CB updraft. The parcel paths exhibit some similarities, although there are also some slight differences related to storm structure. In both cases, the parcels make nearly an entire revolution around the eyewall, both in an earth-relative and a storm-relative sense. For Dean, they make over a full orbit and begin moving away from the storm in the outflow by the end of the period, while for Bill they have almost completed a full orbit by the end of 2 h, and are also moving away in the outflow. These orbital periods are larger than the 40-min period of a convective feature tracked around the eyewall of Hurricane Rita by Fierro et al. (2011) [and a similar period observed in Tropical Storm (TS) Erin (2001) by Griffin et al. (2014)]. This difference is likely due to the fact that the eye radius was 14 km for Rita, but was 38 (54) km for the Dean (Bill) simulation. In fact, assuming the same CB translation speed from Rita ($\sim$36.7 m s$^{-1}$) for the CBs in this study gives a predicted orbital period of 108 (154) min for Dean (Bill), close to the values seen in the trajectories (if slightly high because of not accounting for a different translation speed). Most of the parcels are rapidly accelerated

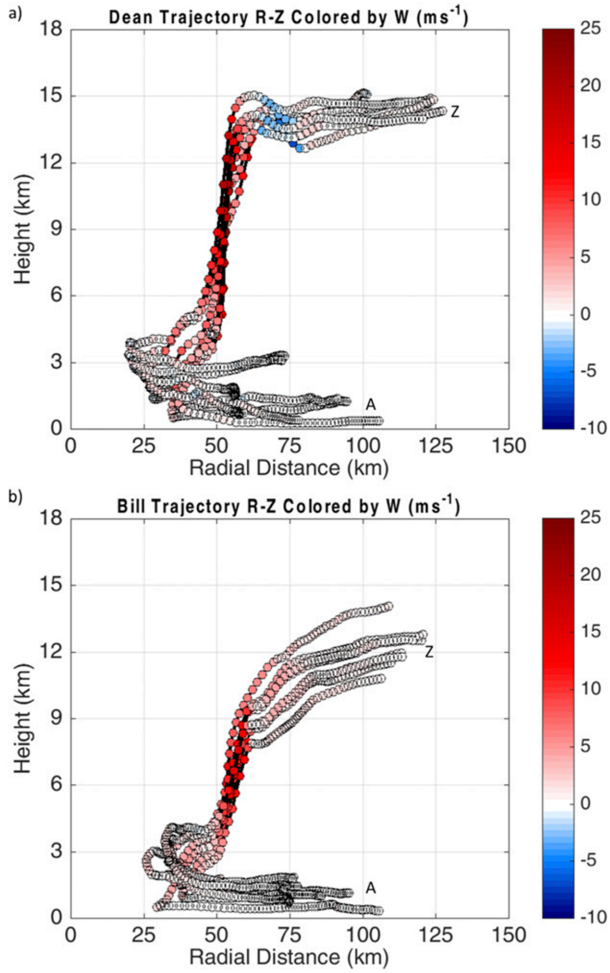


FIG. 14. (a) Paths of eight parcels (the parcel at each initiation height reaching maximum vertical velocity) in storm-relative radius–height space calculated forward 1 h and backward 1 h, centered at hour 98.50 of the Dean simulation. The letter A marks the start of the trajectories and the Z marks the end. The trajectory paths are shaded by the vertical velocity (m s$^{-1}$). (b) As in (a), but for hour 112.50 of the Bill simulation.

outward into the eyewall [perhaps by outflow due to mesovortices or supergradient flow in the eyewall (e.g., Shea and Gray (1973); Smith et al. (2009)], and then ascend quickly in the CB updraft before moving outward in the outflow. The top of the updraft was around 12–14 km for Dean and 10–12 km for Bill, consistent with the vertical velocity differences observed. These paths are generally consistent with the trajectories of Marks and Houze (1987) and Braun (2002). The next section examines the source points of these and some of the other trajectories, based on the back trajectories.

### 2) Parcel origination

Figure 12 shows that many of the trajectories were in the warm core and clear air of the eye at $t = 0$ (hour 98.50 for Dean and hour 112.50 for Bill). However, Fig. 14 shows that most of the maximum-$W$ parcels appear to start out (based on the back trajectories) outside the eyewall, at a radius of 75–100 km. Thus, we next wanted to examine whether these parcels that later formed part of the CB updraft had been part of the eye for a long period of time (e.g., Cram et al. 2007), or only briefly mixed with the eye air (e.g., Braun 2002). This was done by examining the back trajectories at $t = -1$ h (hour 97.50 for Dean and hour 111.50 for Bill) and $t = -30$ min (hour 98.00 for Dean and hour 112.00 for Bill) and their locations relative to the warm core in the eye. For clarity, only the parcels that eventually reached the CB threshold for vertical velocity above 6 km were included. The results are shown in Fig. 15.

Figure 15 shows that all of the parcels that end up in the CB originate well outside the eye and are still outside the eye (although slowly being pulled inward) 30 min before moving into the eyewall updraft. This is true for both the Dean and Bill simulations. Thus, although the outflow occurring within the clear air and warm core does imply eye–eyewall exchange, most of the parcels appear to only briefly mix with the air inside the eye. It may still acquire some buoyancy through this mixing, or, as Braun (2002) showed, most of the buoyancy may come from surface fluxes as the parcel moves inward.

## 4. Conclusions and future work

The results presented here provide insight into the development of CBs, particularly in the eyewall region. The composite figures highlight many structural features that are commonly observed in CBs. The CB distributions are consistent with Black et al. (2002) and Reasor et al. (2013), showing a tendency for CBs to be in the downshear/downshear-left region, especially as the deep-layer shear increases. This result gives confidence that, at least in an aggregate sense, the physical representation of CB development is realistic in these simulations, making them useful for studying smaller-scale processes that are difficult to observe. The composites show that locations with CBs inside $RMW_{6–12}$ tend to have structures that are not apparent in the non-CB composites, including deep, strong radial inflow in the lowest 1–2 km as well as stronger outflow from $z = 12$ to 15 km and outflow from the eye into the eyewall around $z = 2$–4 km.

The individual features examined based on the composites highlight several structures that are important in CB development. Some of these have been previously discussed as a general mechanism for generating eyewall updrafts (e.g., Braun et al. 2006; Braun and Wu 2007;

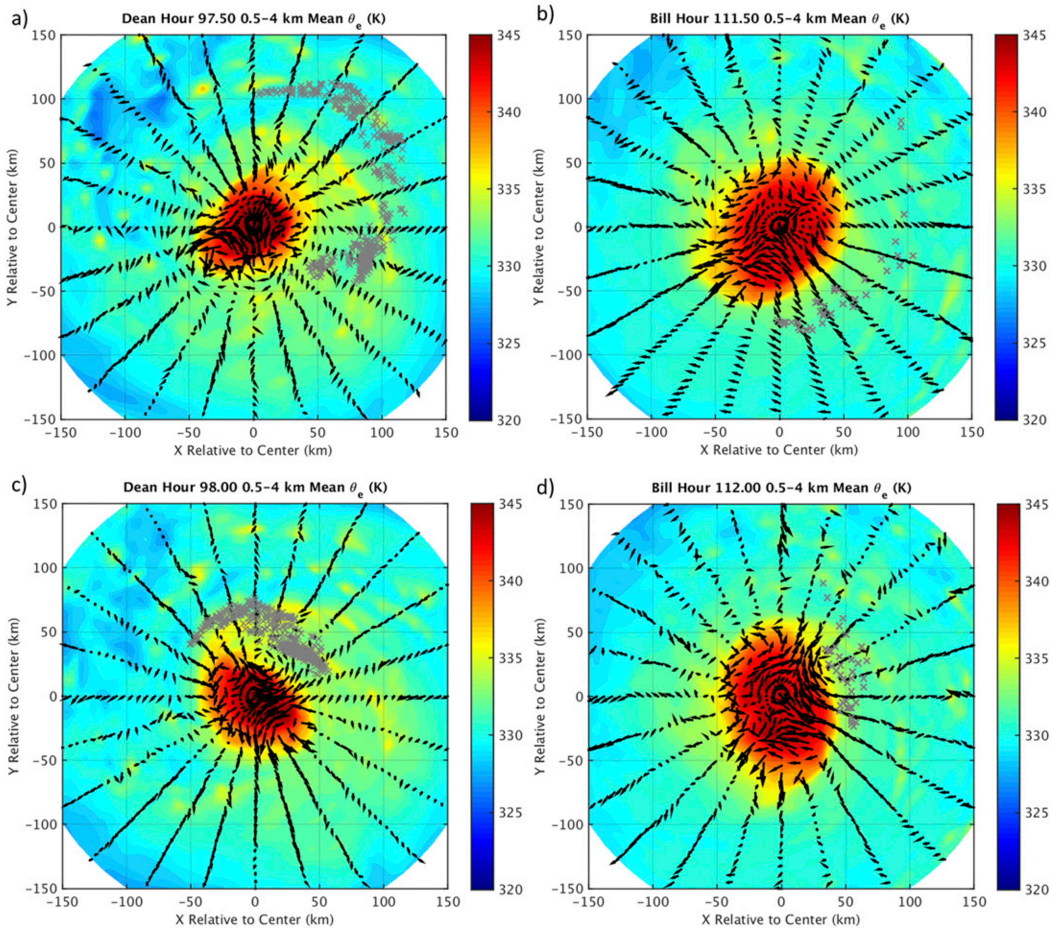


FIG. 15. (a) The 0.5–4-km mean $\theta_e$ (K, shading), 2-km asymmetric wind vectors, and trajectory locations at hour 97.50 of the Dean simulation. (b) As in (a), but for hour 111.50 of the Bill simulation. (c) As in (a), but for hour 98.00. (d) As in (b), but for hour 112.500.

Nguyen et al. 2011) but not specifically tied to CBs, while others have been hinted at but not explored in detail. The first structural mechanism examined was the low-level radial convergence. This mechanism is of particular interest because it has the potential to explain CB development both inside and outside the RMW, as speculated upon in Rogers et al. (2015, 2016). Convergence in the simulations was associated with CB development both in the eyewall and outer bands of the simulated TCs, as shown through correlations as well as the case study comparison. The radial flow anomalies and associated convergence appear to be a key forcing for CBs, and also grow as a CBs develops, increasing the feedback process.

The analysis of asymmetric vorticity revealed another dynamical structural factor that can lead to the growth of CBs: an asymmetric eyewall. Schubert et al. (1999) and Kossin and Schubert (2001) describe a mechanism for the formation of eyewall asymmetric vorticity, based on a breakdown of a barotropically unstable eyewall. Nguyen et al. (2011) discussed a similar process known as ''vacillation cycles'' in eyewall vorticity. Here, asymmetric vorticity was found to be a key factor in CB development, especially for Dean. This finding is consistent with the observations of CB development due to asymmetric vorticity in Hurricane Karl by Guimond et al. (2016), and also the development of eyewall updrafts due to mesovortices in Braun et al. (2006) and Braun and Wu (2007). As the CB distributions here showed, there was no apparent wavenumber-1 asymmetry for Dean, likely because of the overall lower deep-layer shear. Thus, it makes sense that higher-order asymmetries would play a major role, by forcing radial convergence and aiding in outflow from the eye to the eyewall. In contrast, the Bill simulation experienced higher vertical shear, particularly later in the simulation. Thus, a wavenumber-1 asymmetry was more prominent (e.g., Braun and Wu 2007).

The comparisons of decaying and intensifying CBs further highlighted some of the mechanisms discussed above. In addition, it provided further insights into the development of CBs relative to the shear-relative flow. The CBs tended to grow in the downshear and left-of-shear region and then decay upshear. Braun et al. (2006) and Braun and Wu (2007) described how mesovortices and associated updrafts tend to grow downshear and weaken upshear because of the shear-relative flow. This mechanism seems to apply even to the most extreme updrafts (CBs). A major reason for this weakening is the change from low-level inflow in the downshear region to outflow in the upshear region. The anomalous inflow downshear helps to promote low-level convergence. In the composites here, there is strong low-level inflow for the intensifying CBs, pulling parcels into the eye, with weak outflow much more prominent in the decaying phase. The inflow tends to be maximized just before the maximum in vertical velocity. Differences are also seen between the growing and decaying CBs in the radial flow around 12–13-km altitude. The decaying CBs actually have stronger outflow at 12 km, but the inflow due to air recirculating into the eye is stronger for the growing CBs, and in fact is weak to nonexistent in the decaying CBs. The largest difference, however, is seen in the 3–4-km eye-to-eyewall outflow, which also tends to be maximized just before the peak in CB vertical velocity. The analysis of asymmetric flow and reflectivity, $\theta_e$, and vorticity for two of the individual CBs helped cement the idea of eye–eyewall exchange. Outflow was found to start inside the clear and warm eye, and extend into the eyewall, with a ‘‘protrusion’’ of high-$\theta_e$ air extending into the eyewall near the CB in the Dean case. This is consistent with observations of CBs, particularly those of Guimond et al. (2016) in their study of Hurricane Karl (2010).

The CB parcel trajectories provide further evidence of many of the dynamical features described above. Initiated at a height of 0.5–4 km and run backward and forward 1 h, these trajectories provide a unique opportunity to explore both the source region for eyewall CBs as well as the behavior of parcels after ascending. The trajectories originated upwind (with respect to the eyewall winds) from areas of strong asymmetric vorticity where asymmetric wind structure would be expected because of mesovortices. The backward trajectories showed that all of the parcels originated outside of the RMW and moved radially inward at low levels. Many of the parcels were pulled, at least briefly, into the eye of the TC. The forward trajectories from these points inside the RMW then showed that there was outflow from the eye to the eyewall and likely exchange of air between the eye and the eyewall, with the parcels accelerating outward and rising rapidly in the CB updraft, in some cases with W greater than 20 m s$^{-1}$.

This low-level radial outflow, as mentioned above, often appears to be associated with asymmetric radial flow and mixing due to asymmetric vorticity (e.g., Kossin and Eastin 2001; Braun et al. 2006; Braun and Wu 2007). Other possible mechanisms for generating this outflow have been discussed previously. For example, Kepert (2001) and Kepert and Wang (2001) described this radial outflow as a response to gradient wind imbalance generated by low-level inflow of angular momentum, in which the outflow attempts to restore gradient wind balance by advecting angular momentum outward. Montgomery et al. (2014) confirmed the presence of such supergradient flow in the low levels of Hurricane Earl (2010). Similarly, Smith et al. (2009) described a conceptual model for radial flow in the inner core in which the inflow slows down in the inner-core region because of increasing centrifugal and Coriolis forces as the tangential flow becomes supergradient. The air then rises out of the PBL and moves outward until gradient wind balance is attained, at which point it begins to ascend in the eyewall updraft. It is possible that the outflow seen in these simulations also results in some instances from the outflow due to mesovortices, as well as the previously mentioned balanced response to supergradient tangential flow. As this outflow moves outward from the warm core, it can generate buoyancy in the eyewall updrafts (e.g., Guimond et al. 2016). Some of the buoyancy also comes from lower-level parcels warmed by surface fluxes (e.g., Braun 2002).

The calculation of parcel source locations showed that the trajectories started well outside the eye and were only briefly mixed with the eye air before being moved into the CB updraft. Thus, although the outflow of air from the warm core does imply eye–eyewall exchange, it appears as though this air (at least for the limited cases examined here) is mainly inflowing air that briefly mixes with the eye. Although beyond the scope of this study, a deeper examination of parcel buoyancy would prove insightful, as would a larger sample of trajectories for many different CBs in order to determine whether outflow of air that has remained in the eye for a period of time can contribute to eyewall buoyancy (e.g., Cram et al. 2007). Although this mixing of air that has remained in the eye for a long period of time does not appear to be the dominant mechanism in the CBs explored here, it may be important in some CBs (or in TCs with different structures), and an in-depth examination of this topic is a subject of future work.

Figure 16 summarizes the horizontal and vertical structures shown to be important in the development of CBs. Figure 16a shows the horizontal structure. CBs

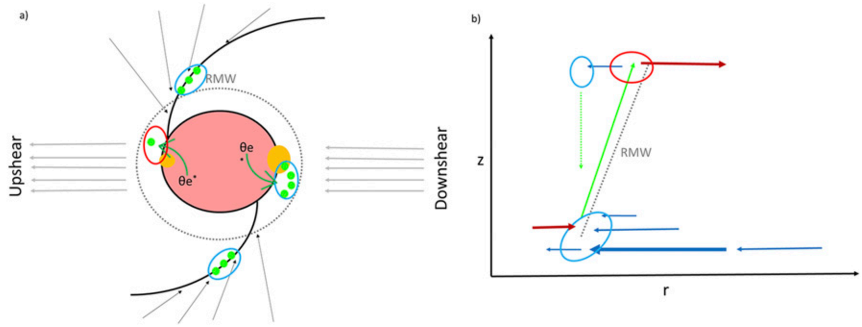


FIG. 16. (a) Schematic illustrating the horizontal structure of the processes that lead to CB development inside and outside the RMW. The dashed gray line represents $RMW_{6–12}$. The pink oval is the eye. The orange circles represent areas of locally enhanced, asymmetric vorticity. The green arrows next to the orange circles represent the asymmetric flow associated with these vorticity anomalies. The gray arrows represent the wavenumber-1 low-level anomalous radial flow due to shear (the upper-level flow is not shown). The black curves outside $RMW_{6–12}$ represent the locations of outer bands or secondary eyewalls, and the black arrows show inflow into these bands. The blue ovals represent areas of anomalous convergence, while the red ovals represent areas of anomalous divergence. Finally, the solid green circles show CB locations. (b) Schematic illustrating the vertical and radial structure of the processes that lead to CB development inside and outside the RMW. The dashed gray line represents $RMW_{6–12}$. The blue arrows indicate radial inflow, with the thickness of the arrows proportional to the magnitude of the flow. The red arrows indicate radial outflow, with the thickness of the arrows again proportional to the strength of the radial velocity. The blue ovals represent areas of radial convergence, while the red ovals represent areas of radial divergence. The solid green arrows show the locations of CB updrafts, while the dashed green arrow shows the location of downdrafts.

inside the RMW are associated with areas of anomalous vorticity (mesovortices), which lead to enhanced low-level radial convergence, particularly in the downshear region where there is background asymmetric low-level inflow (e.g., Braun et al. 2006; Braun and Wu 2007). Upshear, the background asymmetric outflow does not promote low-level convergence. The anomalous cyclonic flow due to the mesovortices also causes low-level outflow from the eye into the eyewall, injecting high-$\theta_e$ air into the eyewall. Outside the RMW, radial bands and secondary eyewalls form, and the convergence of the radial inflow leads to CB formation. Figure 16b illustrates these processes within an $r$–$z$ framework. The radial inflow is strongest in the PBL, and inside the RMW. The outflow promotes radial convergence and also feeds the CB with air mixed between the eye and the eyewall. Aloft, air diverges at the top of the CBs, leading to radial outflow outside the RMW, with radial inflow and compensating subsidence inside the eye. Although the wavenumber-1 asymmetry was more prominent in Bill as a result of higher shear, the results indicate that this conceptual model also remains valid in a variety of shear environments.

These results address the question raised earlier of what mechanisms govern the development of extreme updrafts in the TC core. Extreme eyewall updrafts are closely linked to horizontal asymmetries, especially mesovortices, which induce asymmetries in radial flow. These asymmetries force convergence, which helps to initiate CBs in the eyewall. Convergence and asymmetry in the outer bands of the TC lead to CBs forming radially outward from the eyewall. Composites show that outflow from the eye to the eyewall is a prominent feature in CB development, separate from shear-induced asymmetry. This feature is especially prominent in growing CBs. The differences between Dean and Bill highlight the fact that shear-induced asymmetries are a large part of CB forcing when the shear is strong, but when the shear is weak, higher-order forcing (e.g., mesovortices) dominates.

Future work (beyond the further exploration of eye–eyewall mixing already discussed) could continue to explore hypotheses related to CB development. In particular, understanding the CB formation outside the RMW, specifically how CBs form in secondary eyewalls, would be useful for forecasting during structure transitions. The location of radial convergence seems to play a significant role in regulating CB distributions, and examining the cause of this convergence (beyond the mesovortices shown here) would be insightful. The role of anomalous outflow due to supergradient flow could also be used to investigate the radial location of CB formation. It would be useful to use a larger sample of growing and decaying CBs, including multiple storms of different intensities. In addition, exploring CB development in weaker storms or more hostile environments would prove useful for understanding the role of CBs throughout the entire distribution of TC intensity and structure. It should be noted that these simulations did not remove the impact of the diurnal cycle on TC convection (Dunion et al. 2014), but rather focused on more small-scale changes. However, it would be helpful in a future simulation to examine whether the diurnal cycle impacts CB development or is negligible compared to other asymmetries. It would be worthwhile to explore the impact of model resolution on CB development, and to see how the trajectories and forcing mechanisms change with higher horizontal and temporal resolution. Also, the analyses here focus on upper-level updrafts, but the impact of updrafts in the PBL on boundary layer spinup of the TC would be another interesting research avenue to explore further (e.g., Smith et al. 2015). Finally, CBs could be used as a metric to evaluate the predictions of inner-core structure in numerical simulations of tropical cyclones, particularly for cases where observational data are available.

*Acknowledgments.* The authors thank the staff of the FSU Research Computing Center for their assistance with troubleshooting the simulations, and for providing the high-performance computing resources for the simulations. The comments of three anonymous reviewers led to improvements on an earlier version of the manuscript. ATH was supported by the FSU Legacy Fellowship.

REFERENCES

Aberson, S. D., M. T. Montgomery, and M. L. Black, 2004: A record wind measurement in Hurricane Isabel: Direct evidence of an eyewall mesocyclone? *26th Conf. on Tropical Meteorology*, Miami, FL, Amer. Meteor. Soc., 5D.6. [Available online at https://ams.confex.com/ams/pdfpapers/75718.pdf.]

Avila, L. A., 2009: Tropical cyclone report Hurricane Bill (AL032009). National Hurricane Center, 17 pp. [Available online at www.nhc.noaa.gov/data/tcr/AL032009_Bill.pdf.]

Barnes, G. M., and P. Fuentes, 2010: Eye excess energy and the rapid intensification of Hurricane Lili (2002). *Mon. Wea. Rev.*, **138**, 1446–1458, doi:10.1175/2009MWR3145.1.

Black, M. L., J. F. Gamache, F. D. Marks Jr., C. E. Samsury, and H. E. Willoughby, 2002: Eastern Pacific Hurricanes Jimena of 1991 and Olivia of 1994: The effect of vertical shear on structure and intensity. *Mon. Wea. Rev.*, **130**, 2291–2312, doi:10.1175/1520-0493(2002)130<2291:EPHJOA>2.0.CO;2.

Bolton, D., 1980: The computation of equivalent potential temperature. *Mon. Wea. Rev.*, **108**, 1046–1053, doi:10.1175/1520-0493(1980)108<1046:TCOEPT>2.0.CO;2.

Braun, S. A., 2002: A cloud-resolving simulation of Hurricane Bob (1991): Storm structure and eyewall buoyancy. *Mon. Wea. Rev.*, **130**, 1573–1592, doi:10.1175/1520-0493(2002)130<1573:ACRSOH>2.0.CO;2.

——, and L. Wu, 2007: A numerical study of Hurricane Erin (2001). Part II: Shear and the organization of eyewall vertical motion. *Mon. Wea. Rev.*, **135**, 1179–1194, doi:10.1175/MWR3336.1.

——, M. T. Montgomery, and Z. Pu, 2006: High-resolution simulation of Hurricane Bonnie (1998). Part I: The organization of eyewall vertical motion. *J. Atmos. Sci.*, **63**, 19–42, doi:10.1175/JAS3598.1.

——, and Coauthors, 2013: NASA's Genesis and Rapid Intensifications Processes (GRIP) field experiment. *Bull. Amer. Meteor. Soc.*, **94**, 345–363, doi:10.1175/BAMS-D-11-00232.1.

Chen, H., and D. Zhang, 2013: On the rapid intensification of Hurricane Wilma (2005). Part II: Convective bursts and the upper-level warm core. *J. Atmos. Sci.*, **70**, 146–162, doi:10.1175/JAS-D-12-062.1.

——, and S. G. Gopalakrishnan, 2015: A study on the asymmetric rapid intensification of Hurricane Earl (2010) using the HWRF system. *J. Atmos. Sci.*, **72**, 531–550, doi:10.1175/JAS-D-14-0097.1.

——, D. Zhang, and J. Carton, 2011: On the rapid intensification of Hurricane Wilma (2005). Part I: Model prediction and structural changes. *Wea. Forecasting*, **26**, 885–901, doi:10.1175/WAF-D-11-00001.1.

Corbosiero, K. L., and J. Molinari, 2002: The effects of vertical wind shear on the distribution of convection in tropical cyclones. *Mon. Wea. Rev.*, **130**, 2110–2123, doi:10.1175/1520-0493(2002)130<2110:TEOVWS>2.0.CO;2.

Cram, T. A., J. Persing, M. T. Montgomery, and S. A. Braun, 2007: A Lagrangian trajectory view on transport and mixing processes between the eye, eyewall, and environment using a high-resolution simulation of Hurricane Bonnie (1998). *J. Atmos. Sci.*, **64**, 1835–1856, doi:10.1175/JAS3921.1.

Davis, C., and Coauthors, 2008: Prediction of landfalling hurricanes with the Advanced Hurricane WRF model. *Mon. Wea. Rev.*, **136**, 1990–2005, doi:10.1175/2007MWR2085.1.

DeHart, J. C., R. A. Houze Jr., and R. F. Rogers, 2014: Quadrant distribution of tropical cyclone inner-core kinematics in relation to environmental shear. *J. Atmos. Sci.*, **71**, 2713–2732, doi:10.1175/JAS-D-13-0298.1.

Dolling, K. P., and G. M. Barnes, 2012: The creation of a high equivalent potential temperature reservoir in Tropical Storm Humberto (2001) and its possible role in storm deepening. *Mon. Wea. Rev.*, **140**, 492–505, doi:10.1175/MWR-D-11-00068.1.

Draxler, R. R., and G. D. Hess, 1997: Description of the HYSPLIT_4 modeling system. NOAA Tech. Memo. ERL ARL-224, NOAA/Air Resources Laboratory, Silver Spring, MD, 24 pp. [Available online at https://www.arl.noaa.gov/documents/reports/arl-224.pdf.]

——, and ——, 1998: An overview of the HYSPLIT_4 modeling system of trajectories, dispersion, and deposition. *Aust. Meteor. Mag.*, **47**, 295–308.

Dudhia, J., and Coauthors, 2008: Prediction of Atlantic tropical cyclones with the Advanced Hurricane WRF (AHW) model. *28th Conf. on Tropical Meteorology*, Orlando, FL, Amer. Meteor. Soc., 18A.2. [Available online at https://ams.confex.com/ams/28Hurricanes/techprogram/paper_138004.htm.]

Dunion, J. P., C. D. Thorncroft, and C. S. Velden, 2014: The tropical cyclone diurnal cycle of mature hurricanes. *Mon. Wea. Rev.*, **142**, 3900–3919, doi:10.1175/MWR-D-13-00191.1.

Eastin, M. D., W. M. Gray, and P. G. Black, 2005: Buoyancy of convective vertical motions in the inner-core of intense hurricanes. Part II: Case studies. *Mon. Wea. Rev.*, **133**, 209–227, doi:10.1175/MWR-2849.1.

Fierro, A. O., and J. M. Reisner, 2011: High-resolution simulation of the electrification and lightning of Hurricane Rita during the period of rapid intensification. *J. Atmos. Sci.*, **68**, 477–494, doi:10.1175/2010JAS3659.1.

——, R. F. Rogers, F. D. Marks, and D. S. Nolan, 2009a: The impact of horizontal grid spacing on the microphysical and kinematic structures of strong tropical cyclones simulated with the WRF-ARW model. *Mon. Wea. Rev.*, **137**, 3717–3743, doi:10.1175/2009MWR2946.1.

——, J. Simpson, M. A. LeMone, J. M. Straka, and B. F. Smull, 2009b: On how hot towers fuel the Hadley cell: An observational and modeling study of line-organized convection in the equatorial trough from TOGA COARE. *J. Atmos. Sci.*, **66**, 2730–2746, doi:10.1175/2009JAS3017.1.

——, X. Shao, T. Hamlin, J. M. Reisner, and J. Harlin, 2011: Evolution of eyewall convective events as indicated by intracloud and cloud-to-ground lightning activity during the rapid intensification of Hurricanes Rita and Katrina. *Mon. Wea. Rev.*, **139**, 1492–1504, doi:10.1175/2010MWR3532.1.

——, E. R. Mansell, D. R. MacGorman, and C. Ziegler, 2015: Explicitly simulated electrification and lightning within a tropical cyclone based on the environment of Hurricane Isaac (2012). *J. Atmos. Sci.*, **72**, 4167–4193, doi:10.1175/JAS-D-14-0374.1.

Franklin, J. L., 2008: Tropical cyclone report Hurricane Dean (AL042007). National Hurricane Center, 23 pp. [Available online at www.nhc.noaa.gov/data/tcr/AL042007_Dean.pdf.]

Griffin, E. M., T. J. Schuur, D. M. MacGorman, M. R. Kumjian, and A. O. Fierro, 2014: A polarimetric and electrical analysis of the overland reintensification of Tropical Storm Erin (2007). *Mon. Wea. Rev.*, **142**, 2321–2344, doi:10.1175/MWR-D-13-00360.1.

Guimond, S. R., G. M. Heymsfield, and F. J. Turk, 2010: Multiscale observations of Hurricane Dennis (2005): The effects of hot towers on rapid intensification. *J. Atmos. Sci.*, **67**, 633–654, doi:10.1175/2009JAS3119.1.

——, ——, P. D. Reasor, and A. C. Didlake Jr., 2016: The rapid intensification of Hurricane Karl (2010): New remote sensing observations of convective bursts from the Global Hawk platform. *J. Atmos. Sci.*, **73**, 3617–3639, doi:10.1175/JAS-D-16-0026.1.

Halverson, J. B., J. Simpson, G. Heymsfield, H. Pierce, T. Hock, and L. Ritchie, 2006: Warm core structure of Hurricane Erin diagnosed from high-altitude dropsondes during CAMEX-4. *J. Atmos. Sci.*, **63**, 309–324, doi:10.1175/JAS3596.1.

Hazelton, A. T., and R. E. Hart, 2013: Hurricane eyewall slope as determined from airborne radar reflectivity data: Composites and case studies. *Wea. Forecasting*, **28**, 368–386, doi:10.1175/WAF-D-12-00037.1.

——, R. Rogers, and R. E. Hart, 2015: Shear-relative asymmetries in tropical cyclone eyewall slope. *Mon. Wea. Rev.*, **143**, 883–903, doi:10.1175/MWR-D-14-00122.1.

——, R. E. Hart, and R. Rogers, 2017: Analyzing simulated convective bursts in two Atlantic hurricanes. Part II: Intensity change due to bursts. *Mon. Wea. Rev.*, **145**, 3095–3117, doi:10.1175/MWR-D-16-0268.1.

Hendricks, E. A., M. T. Montgomery, and C. A. Davis, 2004: The role of "vortical" hot towers in the formation of Tropical Cyclone Diana (1984). *J. Atmos. Sci.*, **61**, 1209–1232, doi:10.1175/1520-0469(2004)061<1209:TROVHT>2.0.CO;2.

——, B. D. McNoldy, and W. H. Schubert, 2012: Observed inner-core structural variability in Hurricane Dolly (2008). *Mon. Wea. Rev.*, **140**, 4066–4077, doi:10.1175/MWR-D-12-00018.1.

Heymsfield, G. M., J. B. Halverson, J. Simpson, L. Tian, and T. P. Bui, 2001: ER-2 Doppler radar investigations of the eyewall of Hurricane Bonnie during the Convection and Moisture Experiment-3. *J. Appl. Meteor.*, **40**, 1310–1330, doi:10.1175/1520-0450(2001)040<1310:EDRIOT>2.0.CO;2.

Hong, S. Y., Y. Noh, and J. Dudhia, 2006: A new vertical diffusion package with an explicit treatment of entrainment processes. *Mon. Wea. Rev.*, **134**, 2318–2341, doi:10.1175/MWR3199.1.

Iacono, M. J., J. S. Delamere, E. J. Mlawer, M. W. Shephard, S. A. Clough, and W. D. Collins, 2008: Radiative forcing by long-lived greenhouse gases: Calculations with the AER radiative transfer models. *J. Geophys. Res.*, **113**, D13103, doi:10.1029/2008JD009944.

Jorgensen, D. P., E. J. Zipser, and M. A. LeMone, 1985: Vertical motions in intense hurricanes. *J. Atmos. Sci.*, **42**, 839–856, doi:10.1175/1520-0469(1985)042<0839:VMIIH>2.0.CO;2.

Kain, J. S., 2004: The Kain–Fritsch convective parameterization: An update. *J. Appl. Meteor.*, **43**, 170–181, doi:10.1175/1520-0450(2004)043<0170:TKCPAU>2.0.CO;2.

——, and J. M. Fritsch, 1990: A one-dimensional entraining/detraining plume model and its application in convective parameterization. *J. Atmos. Sci.*, **47**, 2784–2802, doi:10.1175/1520-0469(1990)047<2784:AODEPM>2.0.CO;2.

Kelley, O. A., J. Stout, and J. B. Halverson, 2004: Tall precipitation cells in tropical cyclone eyewalls are associated with tropical cyclone intensification. *Geophys. Res. Lett.*, **31**, L24112, doi:10.1029/2004GL021616.

Kepert, J. D., 2001: The dynamics of boundary layer jets within the tropical cyclone core. Part I: Linear theory. *J. Atmos. Sci.*, **58**, 2469–2484, doi:10.1175/1520-0469(2001)058<2469:TDOBLJ>2.0.CO;2.

——, and Y. Wang, 2001: The dynamics of boundary layer jets within the tropical cyclone core. Part II: Nonlinear enhancement. *J. Atmos. Sci.*, **58**, 2485–2501, doi:10.1175/1520-0469(2001)058<2485:TDOBLJ>2.0.CO;2.

Kimball, S. K., and F. C. Dougherty, 2006: The sensitivity of idealized hurricane structure and development to the distribution of vertical levels in MM5. *Mon. Wea. Rev.*, **134**, 1987–2008, doi:10.1175/MWR3171.1.

Kossin, J. P., and M. D. Eastin, 2001: Two distinct regimes in the kinematic and thermodynamic structure of the hurricane eye and eyewall. *J. Atmos. Sci.*, **58**, 1079–1090, doi:10.1175/1520-0469(2001)058<1079:TDRITK>2.0.CO;2.

——, and W. H. Schubert, 2001: Mesovortices, polygonal flow patterns, and rapid pressure falls in hurricane-like vortices. *J. Atmos. Sci.*, **58**, 2196–2209, doi:10.1175/1520-0469(2001)058<2196:MPFPAR>2.0.CO;2.

——, and ——, 2004: Mesovortices in Hurricane Isabel (2003). *Bull. Amer. Meteor. Soc.*, **85**, 151–153, doi:10.1175/BAMS-85-2-151.

——, and M. Sitkowski, 2009: An objective model for identifying secondary eyewall formation in hurricanes. *Mon. Wea. Rev.*, **137**, 876–892, doi:10.1175/2008MWR2701.1.

Malkus, J. S., and H. Riehl, 1960: On the dynamics and energy transformations in steady-state hurricanes. *Tellus*, **12**, 1–20, doi:10.3402/tellusa.v12i1.9351.

Marks, F. D., Jr., and R. A. Houze Jr., 1987: Inner core structure of Hurricane Alicia from airborne Doppler radar observations. *J. Atmos. Sci.*, **44**, 1296–1317, doi:10.1175/1520-0469(1987)044<1296:ICSOHA>2.0.CO;2.

Michalakes, J., J. Dudhia, D. Gill, T. Henderson, J. Klemp, W. Skamarock, and W. Wang, 2005: The Weather Research and Forecast Model: Software architecture and performance. *Proc. 11th Workshop on High Performance Computing in Meteorology*, Reading, United Kingdom, ECMWF, 156–168.

Montgomery, M. T., J. A. Zhang, and R. K. Smith, 2014: An analysis of the observed low-level structure of rapidly intensifying and mature Hurricane Earl (2010). *Quart. J. Roy. Meteor. Soc.*, **140**, 2132–2146, doi:10.1002/qj.2283.

Morrison, H., J. A. Curry, and V. I. Khvorostyanov, 2005: A new double-moment microphysics parameterization for application in cloud and climate models. Part I: Description. *J. Atmos. Sci.*, **62**, 1665–1677, doi:10.1175/JAS3446.1.

Nguyen, C. M., M. J. Reeder, N. E. Davidson, R. K. Smith, and M. T. Montgomery, 2011: Inner-core vacillation cycles during the intensification of Hurricane Katrina. *Quart. J. Roy. Meteor. Soc.*, **137**, 829–844, doi:10.1002/qj.823.

Noh, Y., W. G. Cheon, S. Y. Hong, and S. Raasch, 2003: Improvement of the K-profile model for the planetary boundary layer based on large eddy simulation data. *Bound.-Layer Meteor.*, **107**, 401–427, doi:10.1023/A:1022146015946.

Nolan, D. S., Y. Moon, and D. P. Stern, 2007: Tropical cyclone intensification from asymmetric convection: Energetics and efficiency. *J. Atmos. Sci.*, **64**, 3377–3405, doi:10.1175/JAS3988.1.

——, R. Atlas, K. T. Bhatia, and L. R. Bucci, 2013: Development and validation of a hurricane nature run using the joint OSSE nature run and the WRF model. *J. Adv. Model. Earth Syst.*, **5**, 382–405, doi:10.1002/jame.20031.

Powell, M. D., P. J. Vickery, and T. A. Reinhold, 2003: Reduced drag coefficient for high wind speeds in tropical cyclones. *Nature*, **422**, 279–283, doi:10.1038/nature01481.

Reasor, P. D., R. Rogers, and S. Lorsolo, 2013: Environmental flow impacts on tropical cyclone structure diagnosed from airborne Doppler radar composites. *Mon. Wea. Rev.*, **141**, 2949–2969, doi:10.1175/MWR-D-12-00334.1.

Rogers, R., and Coauthors, 2006: The Intensity Forecasting Experiment: A NOAA multiyear field program for improving tropical cyclone intensity forecasting. *Bull. Amer. Meteor. Soc.*, **87**, 1523–1537, doi:10.1175/BAMS-87-11-1523.

——, P. Reasor, and S. Lorsolo, 2013: Airborne Doppler observations of the inner-core structural differences between intensifying and steady-state tropical cyclones. *Mon. Wea. Rev.*, **141**, 2970–2991, doi:10.1175/MWR-D-12-00357.1.

——, P. D. Reasor, and J. A. Zhang, 2015: Multiscale structure and evolution of Hurricane Earl (2010) during rapid intensification. *Mon. Wea. Rev.*, **143**, 536–562, doi:10.1175/MWR-D-14-00175.1.

——, J. A. Zhang, J. Zawislak, G. R. Alvey, E. J. Zipser, and H. Jiang, 2016: Observations of the structure and evolution of Hurricane Edouard (2014) during intensity change. Part II: Kinematic structure and the distribution of deep convection. *Mon. Wea. Rev.*, **144**, 3355–3376, doi:10.1175/MWR-D-16-0017.1.

Schubert, W. H., and J. J. Hack, 1982: Inertial stability and tropical cyclone development. *J. Atmos. Sci.*, **39**, 1687–1697, doi:10.1175/1520-0469(1982)039<1687:ISATCD>2.0.CO;2.

——, M. T. Montgomery, R. K. Taft, T. A. Guinn, S. R. Fulton, J. P. Kossin, and J. P. Edwards, 1999: Polygonal eyewalls, asymmetric eye contraction, and potential vorticity mixing in hurricanes. *J. Atmos. Sci.*, **56**, 1197–1223, doi:10.1175/1520-0469(1999)056<1197:PEAECA>2.0.CO;2.

Shea, D. J., and W. M. Gray, 1973: The hurricane's inner core region. I. Symmetric and asymmetric structure. *J. Atmos. Sci.*, **30**, 1544–1564, doi:10.1175/1520-0469(1973)030<1544:THICRI>2.0.CO;2.

Skamarock, W. C., and J. B. Klemp, 2008: A time-split nonhydrostatic atmospheric model for research and NWP applications. *J. Comput. Phys.*, **227**, 3465–3485, doi:10.1016/j.jcp.2007.01.037.

Smith, R. K., M. T. Montgomery, and N. V. Sang, 2009: Tropical cyclone spin up revisited. *Quart. J. Roy. Meteor. Soc.*, **135**, 1321–1335, doi:10.1002/qj.428.

——, G. Kilroy, and M. T. Montgomery, 2015: Why do model tropical cyclones intensify more rapidly at low latitudes? *J. Atmos. Sci.*, **72**, 1783–1804, doi:10.1175/JAS-D-14-0044.1.

Stern, D. P., and D. S. Nolan, 2009: Reexamining the vertical structure of tangential winds in tropical cyclones: Observations and theory. *J. Atmos. Sci.*, **66**, 3579–3600, doi:10.1175/2009JAS2916.1.

——, J. R. Brisbois, and D. S. Nolan, 2014: An expanded dataset of hurricane eyewall sizes and slopes. *J. Atmos. Sci.*, **71**, 2747–2762, doi:10.1175/JAS-D-13-0302.1.

Tao, C., and H. Jiang, 2013: Global distribution of hot towers in tropical cyclones based on 11-yr TRMM data. *J. Climate*, **26**, 1371–1386, doi:10.1175/JCLI-D-12-00291.1.

Vigh, J. L., and W. H. Schubert, 2009: Rapid development of the tropical cyclone warm core. *J. Atmos. Sci.*, **66**, 3335–3350, doi:10.1175/2009JAS3092.1.

Willoughby, H. E., J. A. Clos, and M. G. Shoreibah, 1982: Concentric eyewalls, secondary wind maxima, and the evolution of the hurricane vortex. *J. Atmos. Sci.*, **39**, 395–411, doi:10.1175/1520-0469(1982)039<0395:CEWSWM>2.0.CO;2.

Zhang, J. A., and F. D. Marks, 2015: Effects of horizontal diffusion on tropical cyclone intensity change and structure in idealized three-dimensional numerical simulations. *Mon. Wea. Rev.*, **143**, 3981–3995, doi:10.1175/MWR-D-14-00341.1.

——, D. S. Nolan, R. F. Rogers, and V. Tallapragada, 2015: Evaluating the impact of improvements in the boundary layer parameterization on hurricane intensity and structure forecasts in HWRF. *Mon. Wea. Rev.*, **143**, 3136–3155, doi:10.1175/MWR-D-14-00339.1.